J. Fluid Mech. (2003), *vol.* 475, *pp.* 101–145.
DOI: 10.1017/S0022112002002537 Printed in the United Kingdom

The mixing layer over a deep cavity at high-subsonic speed

By NICOLAS FORESTIER, LAURENT JACQUIN† AND PHILIPPE GEFFROY

Fundamental and Experimental Aerodynamics Department, ONERA 8, rue des Vertugadins, 92190 Meudon, France

(Received 6 March 2001 and in revised form 29 July 2002)

The flow over a cavity at a Mach number 0.8 is considered. The cavity is deep with an aspect ratio (length over depth) $L/D = 0.42$. This deep cavity flow exhibits several features that makes it different from shallower cavities. It is subjected to very regular self-sustained oscillations with a highly two-dimensional and periodic organization of the mixing layer over the cavity. This is revealed by means of a high-speed schlieren technique. Analysis of pressure signals shows that the first tone mode is the strongest, the others being close to harmonics. This departs from shallower cavity flows where the tones are usually predicted well by the standard Rossiter's model. A two-component laser-Doppler velocimetry system is also used to characterize the phase-averaged properties of the flow. It is shown that the formation of coherent vortices in the region close to the boundary layer separation has some resemblance to the 'collective interaction mechanism' introduced by Ho & Huang (1982) to describe mixing layers subjected to strong sub-harmonic forcing. Otherwise, the conditional statistics show close similarities with those found in classical forced mixing layers except for the production of random perturbations, which reaches a maximum in the structure centres, not in the hyperbolic regions with which turbulence production is usually associated. An attempt is made to relate this difference to the elliptic instability that may be observed here thanks to the particularly well-organized nature of the flow.

1. Introduction

Transonic cavity flows are characterized by discrete tones due to a feedback mechanism between the growth and convection of instability waves in the shear layer and acoustic disturbances produced by the shear-layer impingement on the downstream edge of the cavity, see Rossiter (1964) and Rockwell & Naudascher (1979). Strong variations of pressure, density and side forces resulting from this flow/acoustic resonance make open cavity flows a generic problem for aero-acoustics, aero-optics and aero-elasticity applications. A large number of open cavity flow computations have been recently undertaken due to the rapid development of unsteady CFD (see e.g. Colonius 2001). Most of the published experimental data are concerned with the characterization of the acoustic environment in, and around cavities, e.g. Krishnamurty (1955), Plumblee, Gibson & Lassiter (1962), Rossiter (1964), Heller & Bliss (1975), Tam & Block (1978), Ahuja & Mendoza (1995) and others. It is one of the purposes of the present paper to describe one of the first databases devoted to the description of the flow field.

† Author to whom correspondence should be addressed: jacquin@onera.fr

The present cavity geometry is characterized by a low aspect ratio $L/D = 0.42$ where L denotes the cavity length in the free-stream direction, and D its depth. As will be seen, this choice leads to a strong two-dimensional organization of the flow, which makes the present data adequate for two-dimensional unsteady simulations. A second data set, based on the same techniques, has also been constructed for a shallower cavity $L/D = 2$, obtained by reducing D and maintaining all other parameters unchanged (Forestier, Geffroy & Jacquin 2000). In the latter case, the flow exhibits strong three-dimensionality. Comparisons with these two databases constitute a challenge for CFD. Beyond this practical objective, such a refined description of the flow field may help to improve our inadequate understanding of the cavity flow physics. The present paper will only focus on the deep cavity, which may be considered as a limiting case with regard to available data which generally concern shallower cavities.

Velocity measurements have been obtained with a LDV system. The phase-averaged technique introduced by Hussain & Reynolds (1970) has been applied to these data. The technique can separate the 'coherent' motion, related to the periodic excitation, from the random fluctuating part. The velocity, $\boldsymbol{u}(\boldsymbol{x}, t)$, is decomposed into three parts: $\boldsymbol{u}(\boldsymbol{x}, t) = \bar{\boldsymbol{u}}(\boldsymbol{x}) + \tilde{\boldsymbol{u}}(\boldsymbol{x}, t) + \boldsymbol{u}'(\boldsymbol{x}, t)$, where $\bar{\boldsymbol{u}}(\boldsymbol{x})$ is the ensemble-average, $\tilde{\boldsymbol{u}}(\boldsymbol{x}, t)$ the cyclic component and $\boldsymbol{u}'(\boldsymbol{x}, t)$ the fluctuating component. The phase-averaged velocity is defined as $\langle \boldsymbol{u}(\boldsymbol{x}, t) \rangle = \bar{\boldsymbol{u}}(\boldsymbol{x}) + \tilde{\boldsymbol{u}}(\boldsymbol{x}, t)$. The remaining fluctuating component should be regarded as a residue characterizing events which are not in phase with the reference signal. In the present case, the phase-averaged velocity has been evaluated by using a reference pressure signal measured at a fixed point in the cavity. Application of this classical technique becomes challenging when considering a high-speed flow such as the present one.

In most cavity flows where self-sustained oscillations are observed, coherent structures are formed after a rapid roll-up of the separated boundary layer, in phase with pressure oscillations. These highly coherent eddies usually form at frequencies lower than the natural shear layer frequency. The same phenomenon is also observed in other flows such as impinging jets, jet screech and edge tones. In the case of high-speed jets impinging on a flat plate, Ho & Nosseir (1981) attributed this formation process of large-scale structures to a 'collective interaction mechanism' described by Ho & Huang (1982). In this regime, the strong sub-harmonic forcing leads to 'by-passing' of the pairing and the vorticity stretching mechanisms which drive the growth of natural or weakly forced mixing layers (Winant & Browand 1974). The Kelvin–Helmholtz eddies merge rapidly due to the forcing and this results in the formation of large-scale structures within small distances. The present experiment seems to confirm that this mechanism could also hold in cavities, as already suggested by Gharib & Roshko (1987).

In canonical mixing layers, once coherent structures are formed through successive pairing of Kelvin–Helmholtz vortices, small-scale fluctuations are usually produced through continual stretching of three-dimensional vorticity in the saddle regions between the vortical structures, see Cantwell & Coles (1983) and Hussain & Hayakawa (1987). This is recognized as the main mechanism responsible for small-scale turbulent production. In particular, high levels of phase-averaged small-scale turbulence production by the Reynolds shear stress are identified in the saddle regions. A different result is obtained here, where the phase-averaged laser Doppler measurements show that the Reynolds shear stress is maximum near the vortex centres. This was also observed by Lyn *et al.* (1995) in the base region of a square cylinder. This indicates that the relationship between coherent structures and small-scale activity is not universal

and should depend on the flow conditions. This is discussed in § 4.2 where a close relation is proposed between small-scale production and the elliptic instability that develops in the strained two-dimensional vortex structures found in this flow.

The paper is organized as follows. The experimental set-up, measurement techniques and post-processing are detailed in § 2. The data are presented in § 3. The acoustic properties of the cavity are discussed in § 3.1 and visualizations of the flow are presented in § 3.2. The Reynolds-averaged properties of the velocity field are detailed in § 3.3. Different aspects of the phase averaged results are then considered. The vorticity field is described in § 3.4 and § 3.5. The energetic properties of the coherent and random parts of the flow are discussed in § 3.6. Finally, § 3.7 presents an analysis of the interaction between the flow and the downstream edge of the cavity. Then, in § 4 some physical features are further discussed, namely the formation of the coherent structures, in § 4.1, and the production of random fluctuations, in § 4.2.

2. Apparatus and experimental procedures

2.1. *Flow parameters*

The experiment was carried out in a continuous wind tunnel equipped with a constant-section channel of $100 \times 120\,\text{mm}^2$ area. The tunnel was supplied with dry atmospheric air and the stagnation conditions were ambient pressure and temperature ($p_i \approx 0.98 \times 10^5$ Pa and $T_i \approx 293\,\text{K}$). The cavity model sketched in figure 1 was located in the floor of the channel and spanned the whole width of the test section. The incoming flow Mach number was controlled by means of a motorized throat and was fixed at $M = 0.8$. The dimensions of the cavity were $L = 50\,\text{mm}$ for the length, $D = 120\,\text{mm}$ for the depth and $W = 120\,\text{mm}$ for the width. Aspect ratios were $L/D = 0.42$ and $D/W = 1$. Boundary layer transition was triggered by a rough band located 200 mm upstream of the cavity. The boundary layer has been characterized at 70 mm and 1 mm upstream of the cavity. In the latter position, the incompressible shape factor and the momentum thickness were estimated as $H_i = 1.3$ and $\theta_0 = 0.65\,\text{mm}$, respectively. The Reynolds number $Re_{\theta_0} = U_e\theta_0/\nu$ was 11 145, where $U_e = 258\,\text{m s}^{-1}$ was the free-stream velocity. The Reynolds number based on the cavity length was about $Re_L = U_eL/\nu \approx 860\,000$.

2.2. *Measurement techniques*

Rapid flow visualizations were made using a schlieren apparatus coupled with a rotating Strobodrum™ type camera. The schlieren set-up used a conventional z-type mirror system with a horizontal knife edge. The light source was a Nanolite™ spark light system controlled by a Strobokin™ generator which generates trains of sparks with controllable frequency and duration. The system was synchronized with the drum rotation to avoid overlapping of images after one revolution. The mechanical shutter was controlled manually for a long exposure time. The film used was Kodak Tmax 100 35 mm exposed at IE800. The image frequency was limited by the maximum drum rotation speed and the capabilities of the spark light (20 000 sparks per s). A sample of result showing a period of the cavity flow oscillation is given in figure 2.

Velocity measurements were obtained with a two-component laser-Doppler velocimeter in forward scattering mode equipped with an IFA 750 system. A Bragg cell unit was used to produce a frequency shift of 40 MHz. The radius of the probe volume was estimated to be $\approx 0.2\,\text{mm}$ while the major axis (in the spanwise direction) was estimated to be 2.5 mm in length. Approach to the walls was generally limited to 0.2 mm. Oil smoke introduced upstream of the test section cavity was used for the

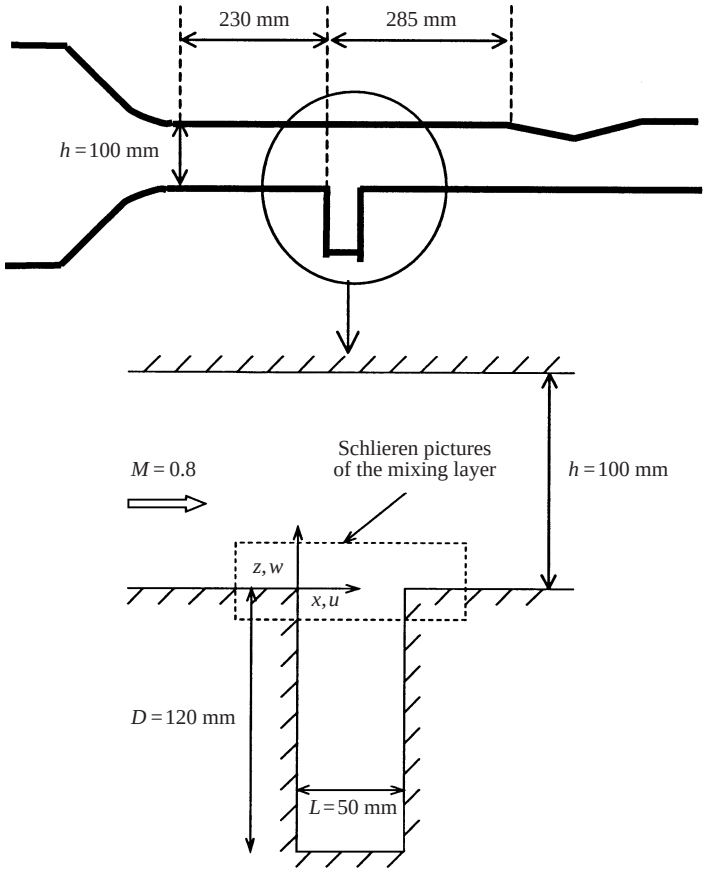

FIGURE 1. Schematic view of the tunnel and the cavity model.

seeding. A typical data rate of 20 kHz was obtained in the shear layer and could be as small as 2 kHz in the central region of the cavity. The level of free-stream turbulence, $\sqrt{\overline{u_0'^2}}/U_e$, measured at $x/L = -1.4$, was 1.5% (where u_0' is the r.m.s. delivered by the LDV system). This is typical of noise in standard LDV systems. More details about the LDV set-up are given in Jacquin, Forestier & Geffroy (1998).

2.3. *Synchronization*

A reference signal delivered by a Kulite^{TM} sensor located 35 mm below the edge of the upstream wall of the cavity was used to obtain the phase-averaged velocity field. Figure 3 shows the pressure signal power spectrum. The spectrum is dominated by the fundamental frequency $f_1 = 1975$ Hz and higher discrete frequencies which are close to its harmonics. The fundamental is the strongest (≈ 155 dB). The acoustics of the cavity will be commented on further in § 3.1.

The fundamental frequency, which is close to 2 kHz, may be compared to the natural, most unstable, frequency of the mixing layers which is found to be close to $f_0 \approx 7$ kHz when considering a Strouhal number $St_\theta = f_0\theta_0/U_c = 0.032$ (see Ho & Huerre 1984) with $\theta_0 = 0.648$ mm and where the convection speed is chosen as $U_c \approx U_e/2 = 129\,\mathrm{m\,s^{-1}}$. Thus, the flow is equivalent to a mixing layer subjected to a low-frequency forcing of high intensity.

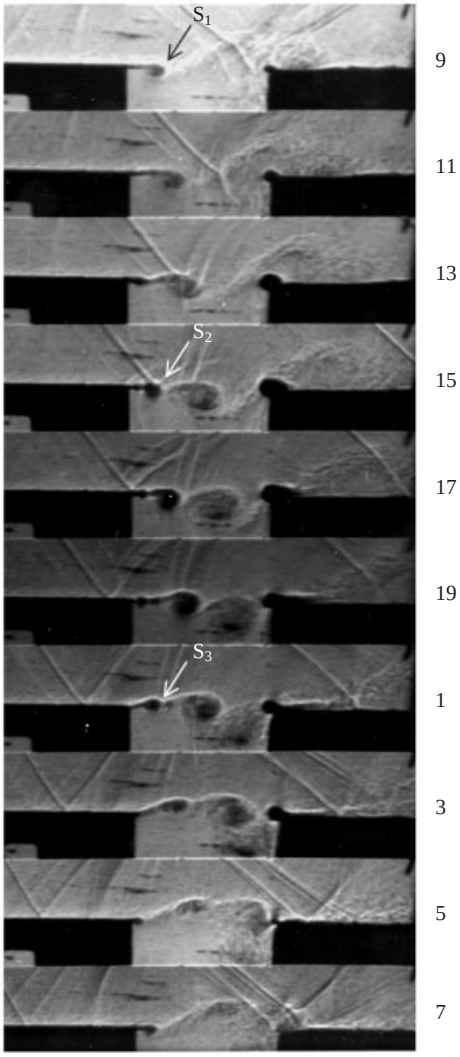

FIGURE 2. High-speed schlieren visualization of one cycle of the mixing layer (20 000 frames per s). Approximate phase numbers are indicated on the right.

As shown in figure 4, the pressure signal was digitized by a PC equipped with a National Instrument EISA A2000 acquisition card operating at a maximum rate of 200 kHz per channel. The signal outputs of the LDV system (photomultipliers) were processed by the IFA controlled by a second PC using the TSI FIND software. Synchronization was controlled by resetting both pressure and the LDV system via an electronic device which received the ADC clock signal from the first PC and generated two pulses. The first pulse reset the IFA internal clock and the second one enabled acquisition of the LDV signals by the IFA. The synchronization between the two clocks was monitored by a second device (Datalink) coupled with the IFA 750.

2.4. *Phase averages*

In order to eliminate high-frequency fluctuations, the pressure signal was low-pass filtered at 3 kHz by means of a digital filter. A peak detection method was used to

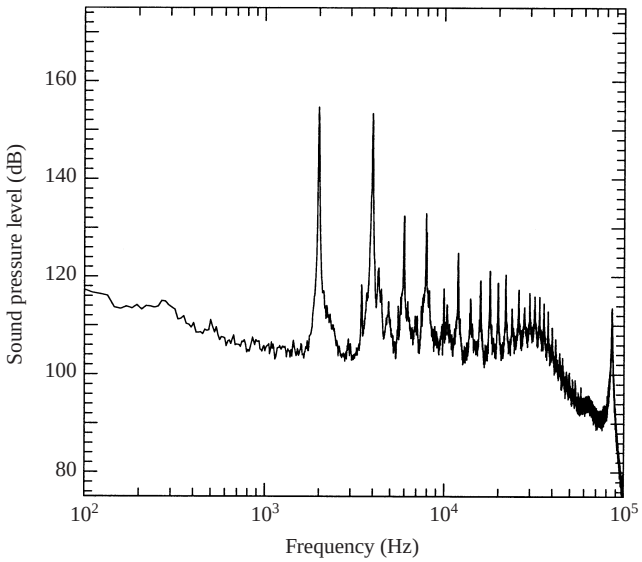

FIGURE 3. Spectrum of the pressure signal delivered by a Kulite transducer located on the upstream vertical wall at $x = 0$, $y = 0$, $z = -35$ mm.

determine the periods in this signal (other possibilities, such as a detection based on gradient maximum, were tested and gave similar results, see Forestier 2000). The construction method of the phase averages is illustrated in figure 5. The instants T_i coinciding with the maximum of the positive values of the pressure, labelled P_1, were determined and stored in a file, see figure 5(a). The mean period was defined as

$$T = \frac{1}{N_T} \sum_{i=1}^{N_T} (T_{i+1} - T_i),$$

where N_T was the total number of periods. The working signal U (e.g. a velocity component), figure 5(b), was then divided into portions delimited by the time references T_i which were superposed on a single period of duration T after compression or dilatation. Variations of the period $(T_{i+1} - T_i)$ were found to be very weak, the r.m.s. being $\sqrt{(T_{i+1} - T_i - T)^2}/T \approx 0.7\%$. Then, T was divided into $N_b = 20$ time intervals or bins, see figure 5(c). The phase average of the signal U corresponds to an ensemble average of U in the interval $[t_n - \tau/2; t_n + \tau/2]$, $1 \leqslant n \leqslant N_b$ where the interval width, τ, can be varied. We use $\tau = T/N_b$, but we have checked that reducing this value did not modify significantly the statistics once τ was large enough to obtain enough samples per bin for accurate statistical convergence (see below). From now on, a phase will denote a given time interval or bin.

The flow fundamental frequency $f_1 \approx 2$ kHz, whereas the characteristic signal sampling rate delivered by the LDV system was about 20 kHz in the mixing layer and could decrease down to 2 kHz in the centre of the re-circulation region inside the cavity, due to a decrease of seeding particle concentration. In the mixing layer, this gave an average of 10 samples per period. For each measurement, 50 000 samples were stored. This corresponds typically to $N_T = 5000$ to 8000 periods, depending on the measurement point. Consequently, each one of the 20 bins contained an average of 2500 samples with variations between 1000 and 3000. We have reduced the length of the bins to a constant value, chosen as the minimum value among the 20 bins. This

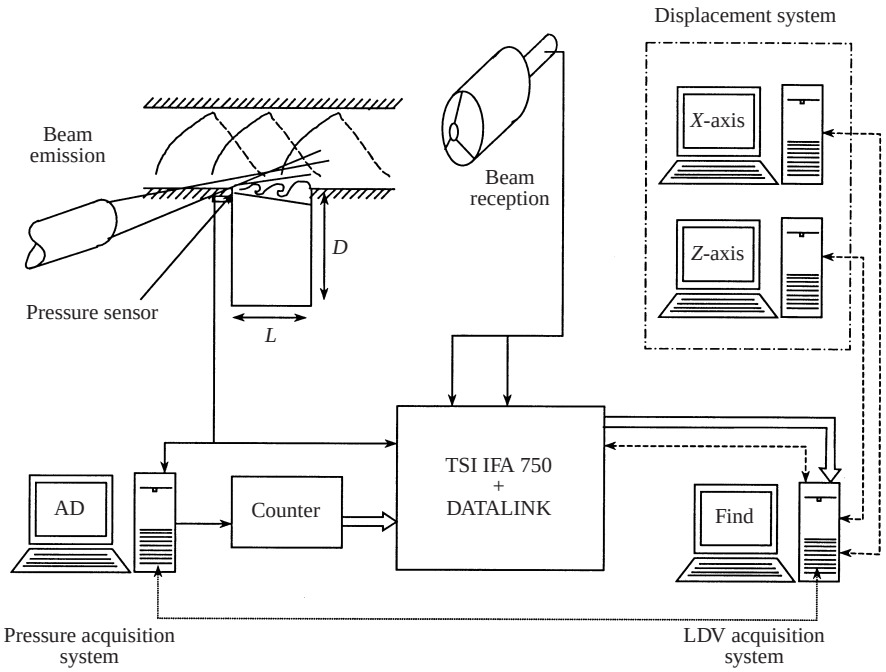

FIGURE 4. Schematic diagram of the synchronized acquisition system.

minimum value varied from point to point within the flow, but was never smaller than 1000 particles so that the total final data contained at least 20 000 particles.

Let $N = \sum_{n=1}^{N_b} N_n$ be the total sample size, where N_n denotes the number of samples in the nth bin. The phase average and the total ensemble average are respectively defined by

$$\langle u(\boldsymbol{x}, t)\rangle = \langle u\rangle(\boldsymbol{x}, n) = \frac{1}{N_n}\sum_{i=1}^{N_n} u(\boldsymbol{x}, t_i), \tag{1}$$

$$\overline{\langle u\rangle}(\boldsymbol{x}) = \frac{1}{N_b}\sum_{n=1}^{N_b} \langle u\rangle(\boldsymbol{x}, n). \tag{2}$$

Note that, due to the above-mentioned variations in the number of samples in each interval, N_n, the ensemble average on the N_b phases $\overline{\langle u\rangle}(\boldsymbol{x})$ would not be equivalent to the temporal average, $\bar{u}(\boldsymbol{x}) = (1/N)\sum_{i=1}^{N} u(\boldsymbol{x}, t_i)$, used when performing standard evaluation of Reynolds-averaged statistics. This velocity bias, which is eliminated here thanks to the conditional analysis, could not have been avoided by other means.

Detailed analyses have shown that a satisfactory convergence of the second-order statistics is obtained for interval sample lengths of 500–1000 particles (Forestier, Geffroy & Jacquin 1999). This may be compared with the 1024 samples per interval used by Cantwell & Coles (1983) for their hot-wire conditional measurements, and with 300 to 500 samples per interval used by Lyn & Rodi (1994) for LDV conditional measurements.

The periodic and random components of the signal are defined by

$$\tilde{u}(x, t) = \langle u(x, t)\rangle - \overline{\langle u\rangle}(x), \quad u'(x, t) = u(x, t) - \langle u(x, t)\rangle. \tag{3}$$

The triple decomposition is then $u(\boldsymbol{x}, t) = \bar{u}(\boldsymbol{x}) + \tilde{u}(\boldsymbol{x}, t) + u'(\boldsymbol{x}, t)$, with $\bar{u}(\boldsymbol{x}) = \overline{\langle u\rangle}(\boldsymbol{x})$.

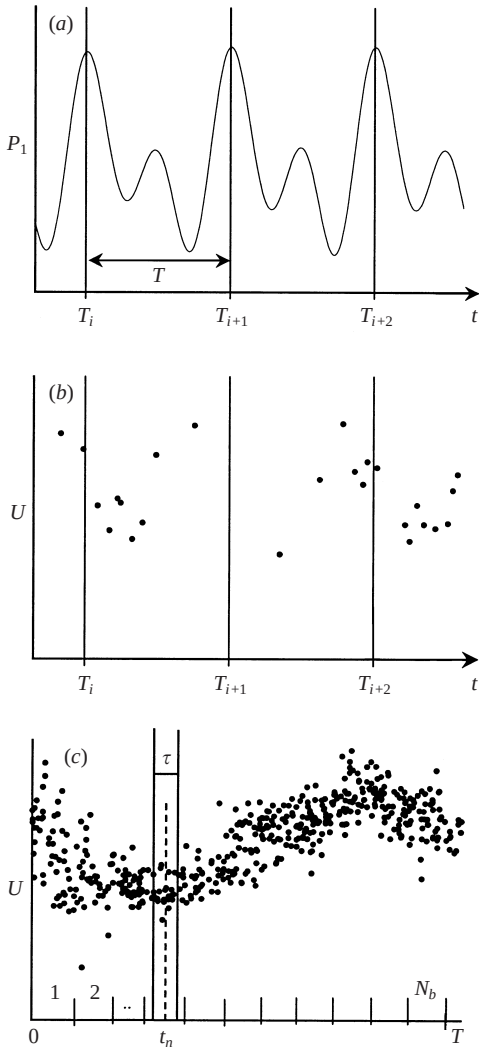

FIGURE 5. Phase average of an LDV signal, U, using a pressure signal P_1. N_b is the number of time intervals or bins and T the mean period of the flow cycle.

3. Results

3.1. *Cavity acoustics*

The modes depicted in the power spectrum of figure 3 may be compared to those deduced from Rossiter's equation:

$$f_n = \frac{n - \alpha}{L/a + L/U_c}, \tag{4}$$

where L is the cavity length, a the sound speed in the cavity, U_c the characteristic convection velocity of the vortices, n the cavity mode, and α a delay time ($\alpha < 1$). The period of mode $n = 1$ is nearly equal to the sum of the time a perturbation takes to be convected downstream over the distance L and the time it takes for the acoustic wave to propagate upstream in the cavity. The factor α accounts for an additional delay between the impingement of the convected eddies and the resulting

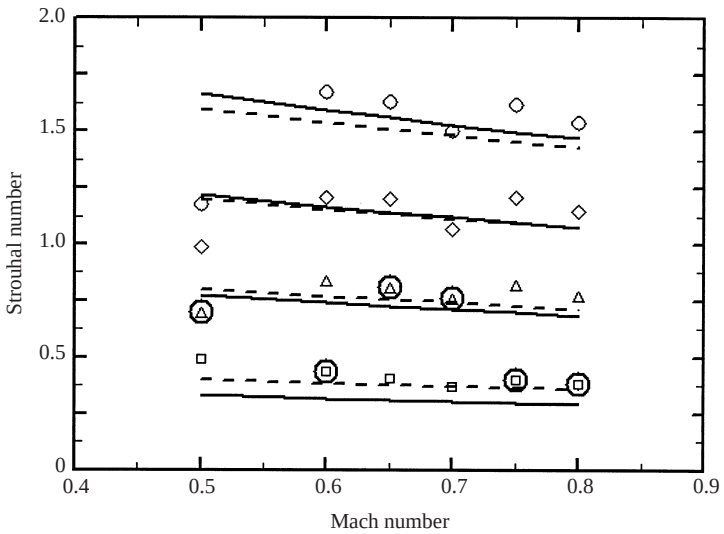

FIGURE 6. Strouhal number versus Mach number. Symbols: experimental results, full line: Rossiter formula (1) with $\alpha = 0.25$, $U_c/U_e = 0.57$, broken line: Rossiter formulae (4) with $\alpha = 0$, $U_c/U_e = 0.50$, circled symbols: strongest modes.

acoustic emission. The ratio U_c/U_e is a second empirical parameter. The hypothesis of a constant convection velocity is a simplification of Rossiter's model. As shown in § 3.4, the convection speed depends on the structure and on its position over the cavity.

Figure 6 shows the variation with the Mach number of the Strouhal number $St = fL/U_e$ corresponding to the first four peaks observed in the pressure spectra. Variations of the Mach number from $M = 0.5$ to $M = 0.8$ have been considered. Continuous lines correspond to Rossiter's formula (4) with $\alpha = 0.25$ and $U_c/U_e = 0.57$. These values, prescribed by Rossiter (1964), are found to fit correctly a large body of published experiments which generally consider narrower cavities, such that $L/D \geqslant 2$. The circled symbols correspond to the strongest mode. Depending on the Mach number, this mode switches from mode 1 to mode 2. Mode 1 is the strongest when $M > 0.7$. The agreement between the Rossiter model, using the standard set of parameters, is not satisfactory. The self-sustained oscillations of the present cavity are closer to harmonics than those observed in shallower cavities. This implies in particular that a smaller delay parameter α must be used in the Rossiter formulae (Rossiter 1964 had already suggested that α decreases with L/D). The results obtained by putting $\alpha = 0$ are plotted in figure 6. Agreement for the first two modes is obtained when taking $U_c/U_e = 0.50$. It turns out that this value corresponds to the averaged velocity of the structure which impacts the downstream edge of the cavity, as will be seen in § 3.4.

From the above results, it may be concluded that the resonant frequencies of the present cavity are not well correlated with the Rossiter model when the standard set of parameter is used. This could be due to the very low value of the aspect ratio, L/D, which makes the present flow different from the shallower cavities which are generally considered.

Also, the possible influence of the tunnel top wall must be also accounted for in the present case where the tunnel height is only two times the cavity length. Kegerise

(1999) has shown that in a cavity of aspect ratio $L/D = 2$, resonance between the Rossiter and vertical duct modes affects the selection of the dominant frequencies. We tested this possibility by comparing, as in Kegerise (1999), the cavity Strouhal numbers shown in figure 6 with those corresponding to the duct modes evaluated using the formulae

$$f_n = \frac{a_e n}{2(D + H)}, \tag{5}$$

where H denotes the tunnel height and a_e the sound speed in the test section. Here, $H = 100\,\text{mm}$. Contrary to Kegerise (1999), we found no correspondence between the strongest cavity modes and resonance between the cavity and the duct modes, when the latter are simply characterized by (5) where effect of the flow in the test section is neglected. A more detailed analysis of propagation and reflection of acoustic wave fronts in the duct is conducted in Appendix A where this mechanism is modelled by the image method. This analysis shows that acoustic fronts travelling upstream may collapse, after reflection, into a coherent wave pattern which is effectively observed in the schlieren pictures (see figures 30 and 31). It is also found that the frequency tones observed in the experiment are close to those corresponding to focusing of reflected waves at a source point located in the cavity region. The model is not in complete agreement with the visualizations but it suggests that the wave propagation resulting from the confinement of the flow by the top wall could contribute, somehow, to modulation of the cavity tones. In particular, such a mechanism is compatible with the promotion of harmonics of the fundamental, as observed here. Specific experimental tests, consisting in changing the geometry of the tunnel and/or using acoustic buffers, as in Kegerise (1999), would be necessary to scrutinise this problem. But this can be also tackled by means of numerical simulations. Results obtained by means of a large-eddy simulation code, which reproduces fairly well the present experiment, indicate that the mixing layer dynamics described in the following sections is hardly sensitive to changes in the tunnel height, see Larchevêque *et al.* (2003). These simulations show that removing the channel top wall damps harmonics of high orders, leaving the two first modes, which dominate the spectrum of figure 3, almost unchanged.

A final remark concerns the possibility of a 'mode switching' phenomenon which has been observed by Cattafesta *et al.* (1998) in a shallower cavity. 'Mode switching' corresponds to a cycle-to-cycle variation of the dominant frequency. In Cattafesta *et al.* (1998), this phenomenon was found to coincide with a variation, from cycle to cycle, of the shear layer structure. This did not occur in our flow, as was checked by applying the same time–frequency analyses as those made by Cattafesta *et al.* (1998), namely short-time Fourier transforms and wavelet transforms. This showed that the hierarchy of the cavity modes does not vary with time. Also, the visualizations described below confirmed that the properties of the flow were very repetitive from cycle to cycle. Finally, it should be remarked that a 'mode switching' would have made the conditional sampling method described above ineffective: we would not have been able to capture a coherent field because all the statistics would have been smeared out. The conclusion is that the present flow is free from 'mode switching'.

3.2. *Mixing layer visualizations*

Figure 2 shows a single cycle of the mixing layer. Flow direction is from left to right. During this cycle, the shear layer rolls up into three distinct vortical structures. The inspection of several hundred periods revealed that the sequence shown in figure 2 was highly repetitive. The schlieren process integrates the density gradient along the flow span. The well-defined structures observed thus reveal the two-dimensional

nature of the flow. Three structures, labelled S_1, S_2 and S_3, are identified. They evolve differently. The first one is captured by the cavity when it approaches the downstream edge. The second impinges on the edge, part penetrating into the cavity, the rest being swept downstream along the horizontal wall. The third structure is ejected into the free stream and does not interact with the edge. This behaviour denotes a strong periodic inflow/outflow process, like that described by Rockwell & Knisely (1979).

An interesting feature of this flow is the presence of a dark bubble on the downstream edge which fluctuates during the cycle. This region corresponds to a high-density-gradient region and can be viewed as an acoustic line source in accordance with models proposed by Bilanin & Covert (1973), Tam & Block (1978) and Zhang & Edwards (1990).

As discussed above, the propagation of acoustic fronts is observed in the cavity and in the external flow region. As explained in Appendix A, these waves correspond to focusing of the acoustic front reflections on the tunnel top wall. Schlieren pictures covering a larger area of the flow are shown and commented on in the Appendix, see figures 30 and 31. Modification of the shear layer dynamics due to impingement by the reflected wave fronts cannot be excluded. As discussed by Doty & McLaughlin (2000), interactions among Mach waves, duct modes and Kelvin–Helmholtz instabilities may occur in compressible mixing layers and may lead to mixing enhancement. However, the optimal conditions given by Doty & McLaughlin (2000) for such an effect are not fulfilled in our flow. The formation of the large-scale structures described above could also be affected by slight boroclinic effects due to interaction of reflected wave fronts with the upstream boundary layer. This may occur after phase 17 in figure 2, when such a front reaches the upstream corner of the cavity. This would concern the formation of structure S_3 (see Larchevêque *et al.* 2003).

3.3. *Characteristic regions of the flow*

The complete data cover conditional LDV measurements performed in several regions whose boundaries are shown in figure 7. The results presented in this paper only consider the two regions where the meshing is visible. One is in the symmetry vertical plane $y = 0$ and has a constant mesh size $\Delta x = \Delta z = 2\,\text{mm}$. The other is in the horizontal plane $z = 0$, with $\Delta x = \Delta y = 5\,\text{mm}$.

The mean longitudinal velocity component, $\overline{U}$, within the vertical measurement region, is shown in figure 8. The shear layer expansion is characterized in figure 9 through the variation of the incompressible momentum thickness, θ, calculated on the mesh shown in figure 7(a) by using the following formula:

$$\theta = \int_{z_{min}}^{z_{max}} \frac{\overline{U}}{U_e}\left(1 - \frac{\overline{U}}{U_e}\right)\mathrm{d}z. \tag{6}$$

Here, z_{min} and z_{max} correspond to the vertical location of the lower and upper mesh boundaries, and U_e denotes the free-stream velocity. The initial momentum thickness measured 1 mm ahead of the upstream cavity edge, $\theta_0 = 0.648\,\text{mm}$, is used for normalizing θ. Relation (6) differs from the standard definition used for free shear layers, i.e. $z_{min} \to -\infty$, $z_{max} \to \infty$. This can lead to differences if $\overline{U}(x, z_{min})$ and/or $\overline{U}(x, z_{max})$ have not reached a constant value. However, considering the regular behaviour of $\overline{U}$ in figure 8, deviations are expected to be small except near the downstream end of the domain where interaction with the wall occurs.

In figure 9, three regions may be defined:

(i) In region I, $0 \leqslant x/\theta_0 \leqslant 17$, the momentum thickness grows linearly with a growth rate equal to 0.12. This value is nearly three times larger than that found in

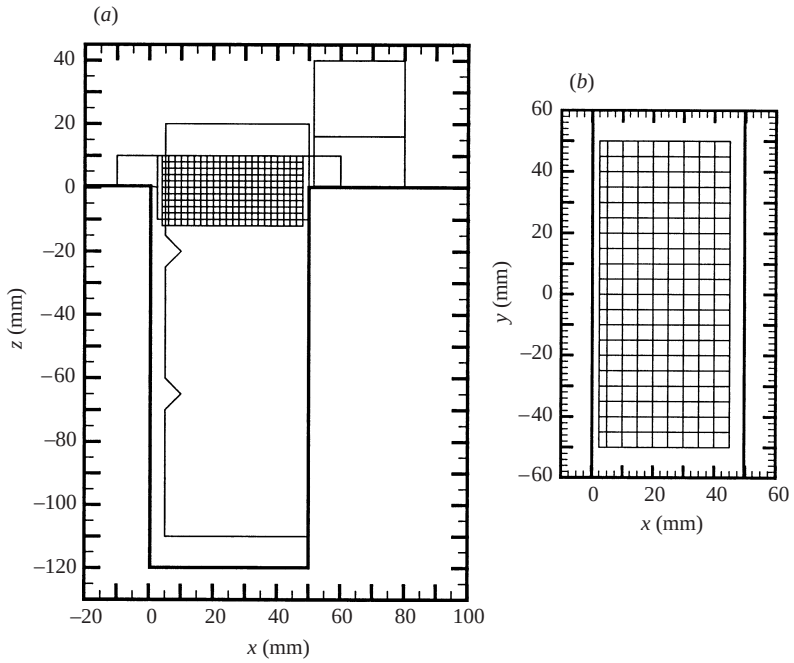

FIGURE 7. Measurement meshes: (*a*) vertical plane $y = 0$, mesh size $\Delta x = \Delta z = 2\,\text{mm}$ in the region where it is detailed; (*b*) horizontal plane $z = 0$, mesh size $\Delta x = \Delta z = 5\,\text{mm}$.

equilibrium free shear layers. A possible interpretation of this high initial spreading rate in the presence of high-amplitude forcing is the 'collective interaction mechanism' described by Ho & Huang (1982). These authors have shown that a high-amplitude forcing of a mixing layer with a frequency one order of magnitude lower than the initial instability frequency leads to the rapid merging of vortices into a single eddy which forms very close to the separation point. As mentioned in the introduction, the 'collective interaction' was also found to participate in the feedback loop of a high-speed subsonic impinging jet, see Ho & Nosseir (1981). The presence of such a mechanism could explain the large coherent structures observed in this flow. As already mentioned by Gharib & Roshko (1987), this could possibly explain the vortex formation observed in cavity flows. This will be discussed further in § 4.

(ii) In region II, $32 \leqslant x/\theta_0 \leqslant 60$, the growth rate decreases to 0.042, a value close to the growth rate of free turbulent mixing layers. As an example, Browand & Trout (1985) found $\mathrm{d}\theta/\mathrm{d}x = 0.034\lambda$ with $\lambda = \Delta U/2\overline{U}$ and $\overline{U}$ the mean velocity of the two flows and ΔU the velocity difference. Neglecting the mean flow recirculation in the cavity leads to $\lambda \approx 1$. Ho (1986) observed that, after a 'collective interaction', the flow of Ho & Huang (1982) resumes a classical growth rate at values of $\lambda x/\theta_0 \approx 20$, which may be compared to $\lambda x/\theta_0 \approx 32$ found in our experiment (with $\lambda \approx 1$). Ho & Huang (1982) observed also a transient damping of the growth rate after the 'collective interaction'. A transition region, $17 \leqslant x/\theta_0 \leqslant 32$, is also observed in figure 9.

The mean velocity profiles and the streamwise component of the turbulent fluctuations in region II are plotted in figure 10 where the similarity variables $\eta = (z - z_{0.5})/\theta(x)$, $\xi = (\bar{u} - \bar{u}_{min})/(\bar{u}_{max} - \bar{u}_{min})$ and $u_0'(\boldsymbol{x})/U_e$ have been used. Here, $z_{0.5}$ denotes the vertical position where $\xi = 0.5$ and u_0' corresponds to the r.m.s. of the streamwise velocity component, $u_0'(\boldsymbol{x}) = \sqrt{\overline{u_0^2(\boldsymbol{x}, t)}}$, when considering the classical

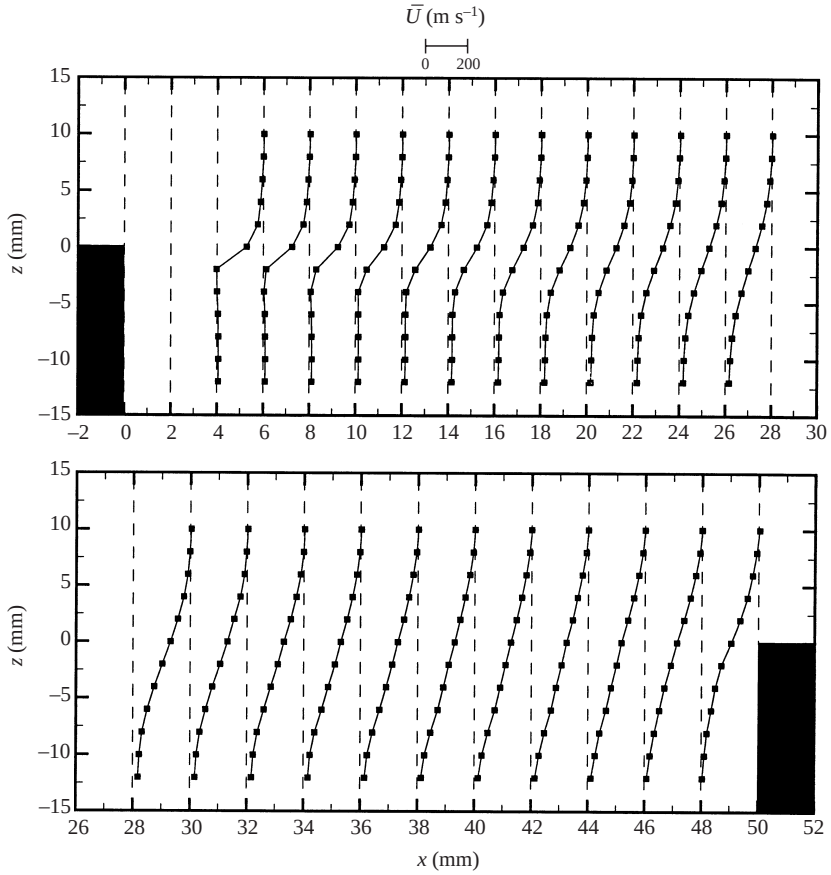

FIGURE 8. Mean velocity profiles: longitudinal velocity component.

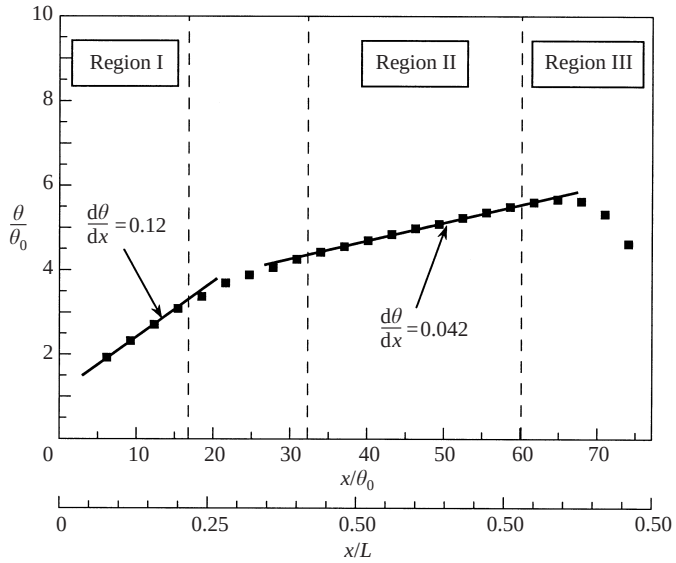

FIGURE 9. Momentum thickness of the mixing layer. θ_0 is the initial momentum thickness at $x = -1$ mm. Dashed lines delimit the three regions defined in § 3.3.

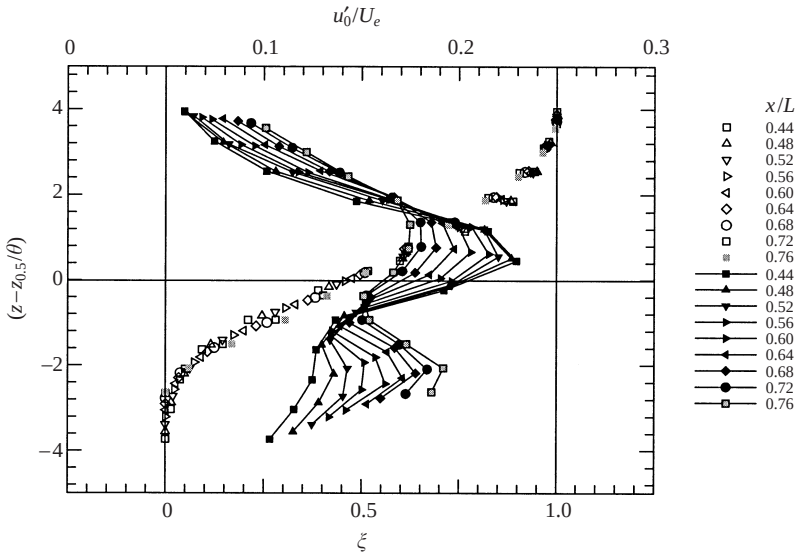

FIGURE 10. Region II: profiles of the mean value (open symbols) and of the r.m.s. (full symbols) of the longitudinal velocity component (suffix '0' denotes standard Reynolds decomposition).

Reynolds decomposition $u(\boldsymbol{x},t)=\bar{u}(\boldsymbol{x})+u_0'(\boldsymbol{x},t)$. From now, suffix '0' will refer to this type of decomposition.

Figure 10 shows that the flow is not self-preserving within region II: the collapse of the mean field (open symbols) is not satisfactory and turbulence profiles exhibit strong variations. In the upper part of the mixing layer, intensity decreases with downstream distance while it increases in the lower part of the mixing layer. Similar two-peak turbulent profiles were observed in a forced mixing layer by Ho & Huang (1982) and Oster & Wygnanski (1982). They were also found in a low-Reynolds-number cavity flow by Gharib & Roshko (1987). Following these authors, such a double-peak profile results from the convection of well-defined vortices at a given frequency inside the measurement domain. Absence of self-similarity in a cavity flow is not surprising. In a free shear layer, Browand & Trout (1985) found that similarity is reached in a non-dimensional distance of about $\lambda x/\theta_0=400$, a value an order of magnitude higher than that corresponding to the beginning of region II.

(iii) In region III, $60\leqslant x/\theta_0\leqslant 77$, the momentum thickness decreases as the flow approaches the downstream edge of the cavity. The extent of region III, which is 17 initial momentum thickness wide, could characterize the influence of the downstream corner. The final decrease of the momentum thickness is spurious. It results from the too small values of z_{min} and z_{max} when applying relation (6) in this region. Region III is characterized by an inflow/outflow motion as shown in figure 11(a) where the vertical velocity profiles $\overline{W}$ are plotted in dimensionless variables. Close to the downstream cavity edge, the flow is subjected to a positive (resp. negative) streamwise gradient of the vertical velocity at positive (resp. negative) vertical positions. This leads to negative (resp. positive) shear stresses in these region, as shown in figure 11(b). According to figure 11(c), this may be interpreted by considering a displaced particle argument, similar to that used to explain why $\overline{u_0'w_0'}$ is negative in a free shear layer. This classical reasoning is based on the hypothesis that an impulsively displaced fluid particle conserves its momentum. In a free shear layer where $\mathrm{d}\overline{U}/\mathrm{d}z>0$, see region I and II in figure 11(c), the fluctuation of the streamwise velocity component of a fluid particle

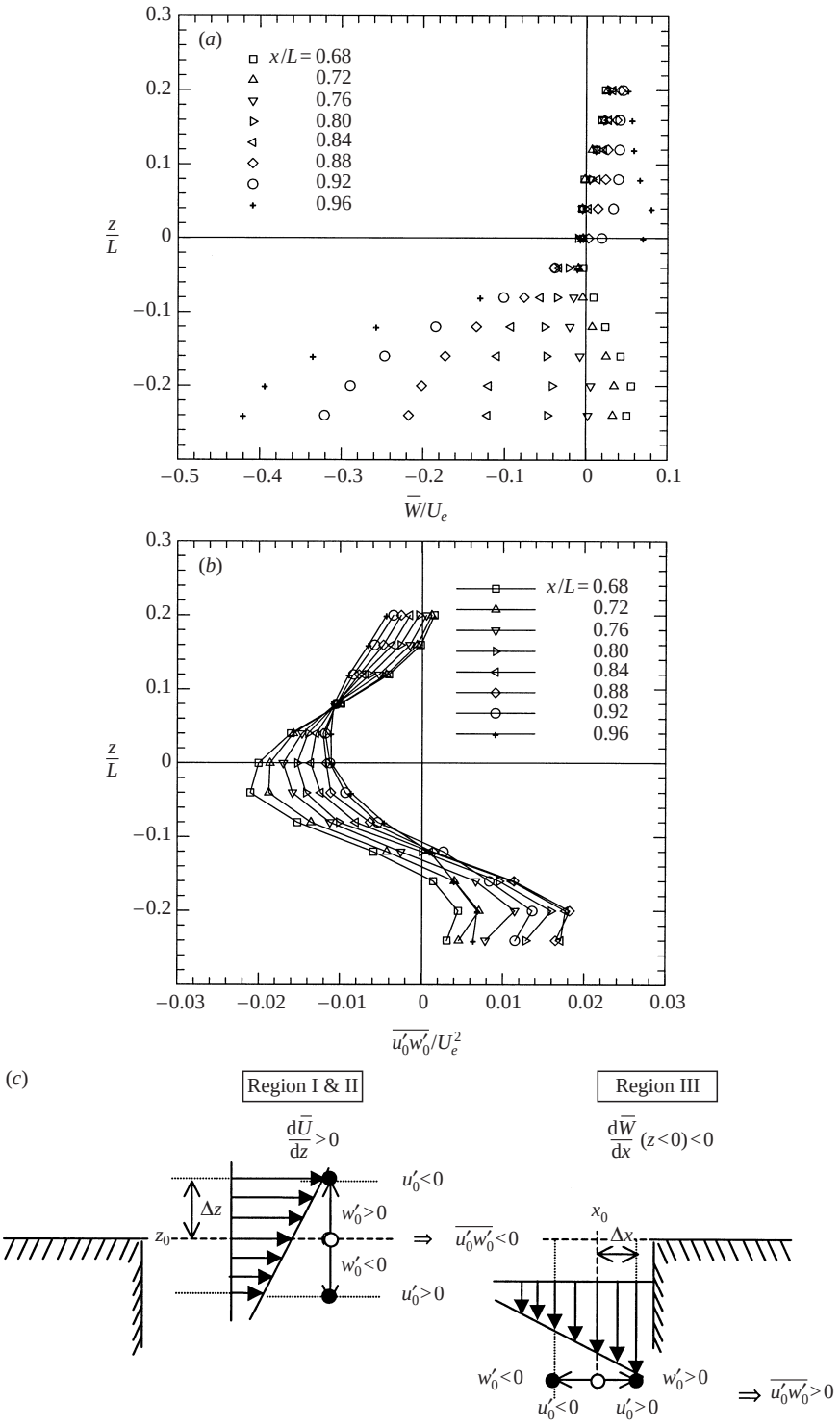

FIGURE 11. Region III: (*a*) profiles of the vertical component of the mean velocity, (*b*) profiles of the shear stress $\overline{u_0'w_0'}$, and (*c*) interpretation of the shear stress sign using a particle displacement argument.

displaced with velocity $w_0' > 0$ is negative, i.e. $u_0' = \overline{U}(z_0) - \overline{U}(z_0 + \Delta z) < 0$. This means that $\overline{u_0' w_0'} < 0$. The same is true for a negative vertical displacement: $w_0' < 0$ gives $u_0' = \overline{U}(z_0) - \overline{U}(z_0 - \Delta z) > 0$. Considering now the region close to the downstream vertical wall (apart from its boundary layer), $\mathrm{d}\overline{W}/\mathrm{d}x(z < 0) < 0$, see figure 11(*a*). A longitudinal impulsive displacement of positive sign, $u_0' > 0$, leads to $w_0' = \overline{W}(x_0) - \overline{W}(x_0 + \Delta x) > 0$, that is $\overline{u_0' w_0'} > 0$. The same conclusion is reached for $u_0' < 0$.

3.4. *The phase-averaged vorticity*

Contours of the phase-averaged spanwise vorticity component, $\langle \Omega_y \rangle$, normalized by the convection time scale, L/U_e, are shown in figure 12(*a–d*). The pictures on the right-hand side show instantaneous schlieren visualizations (see § 3.2), the flow direction being from left to right. Solid lines correspond to positive values and coordinates are normalized by the cavity length. No measurements were possible for $x/L < 0.08$ and $x/L > 0.96$ due to optical constraints. The contour plots of the phase-averaged vorticity look similar to the schlieren pictures. High-vorticity regions correspond to vortical structures observed in the schlieren visualizations, identified as S_1, S_2, S_3; very low vorticity levels are found away of the shear layer (see the values given in the figures). It is important to note that $\langle \Omega_y \rangle$ is deduced from finite-difference formulae and is, consequently, sensitive to the density of the meshing. The values presented herein, which are obtained by using a constant mesh size $\Delta x = \Delta z = 2\,\mathrm{mm}$, underestimate $\langle \Omega_y \rangle$. This has no impact on the present qualitative description.

Variation of the spanwise vorticity peaks is shown in figure 13. The peak values of structures S_1 and S_2 grow in the first region. This could be related to a 'collective interaction' mechanism, as discussed in § 3.3. When travelling through the transition region and through region II, the size of the structures increases and the vorticity peak values decrease. The latter reach asymptotic constant values in region III. Figure 14 compares the location of these maxima with the position of the vorticity centroids, which were evaluated, following Lyn *et al.* (1995), from integration of the vorticity field by using the following relations:

$$x_c = \frac{\sum\limits_{\langle \Omega_y \rangle_{ij} \geqslant \langle \Omega_y \rangle_0} x \langle \Omega_y \rangle_{ij} \Delta S_{ij}}{\sum\limits_{\langle \Omega_y \rangle_{ij} \geqslant \langle \Omega_y \rangle_0} \langle \Omega_y \rangle_{ij} \Delta S_{ij}}, \quad z_c = \frac{\sum\limits_{\langle \Omega_y \rangle_{ij} \geqslant \langle \Omega_y \rangle_0} z \langle \Omega_y \rangle_{ij} \Delta S_{ij}}{\sum\limits_{\langle \Omega_y \rangle_{ij} \geqslant \langle \Omega_y \rangle_0} \langle \Omega_y \rangle_{ij} \Delta S_{ij}}. \tag{7}$$

ΔS_{ij} is a surface element on which the vorticity is $\langle \Omega_y \rangle_{ij}$. The cut-off value, $\langle \Omega_y \rangle_0$, was kept constant and equal to $+5$ whatever the phase considered. As shown in figure 14, good correspondence is found between the centroids and the peak vorticity locations, as in Lyn *et al.* (1995). From figures 12 and 14, it is seen that when structure S_1 penetrates the cavity, its contour levels are smeared. Its peak value shown in figure 13 decreases less than that of the two other structures. Structure S_2 exhibits a nearly horizontal path and figure 13 shows that its vorticity, which is initially the highest, decreases sharply. The third structure, which does not interact with the wall corner, has a smaller size and weaker vorticity. Its vorticity becomes half that of the first structure at the end of region II.

Finally, it can be seen on figure 12 that the three structures do not merge (see also figure 2). This is in agreement with Oster & Wygnanski (1982) who concluded that the pairing process can be delayed or completely inhibited in a forced turbulent mixing layer. The last two frames suggest a merger between structures S_1 and S_2, but is due to the blockage of S_1 by the wall.

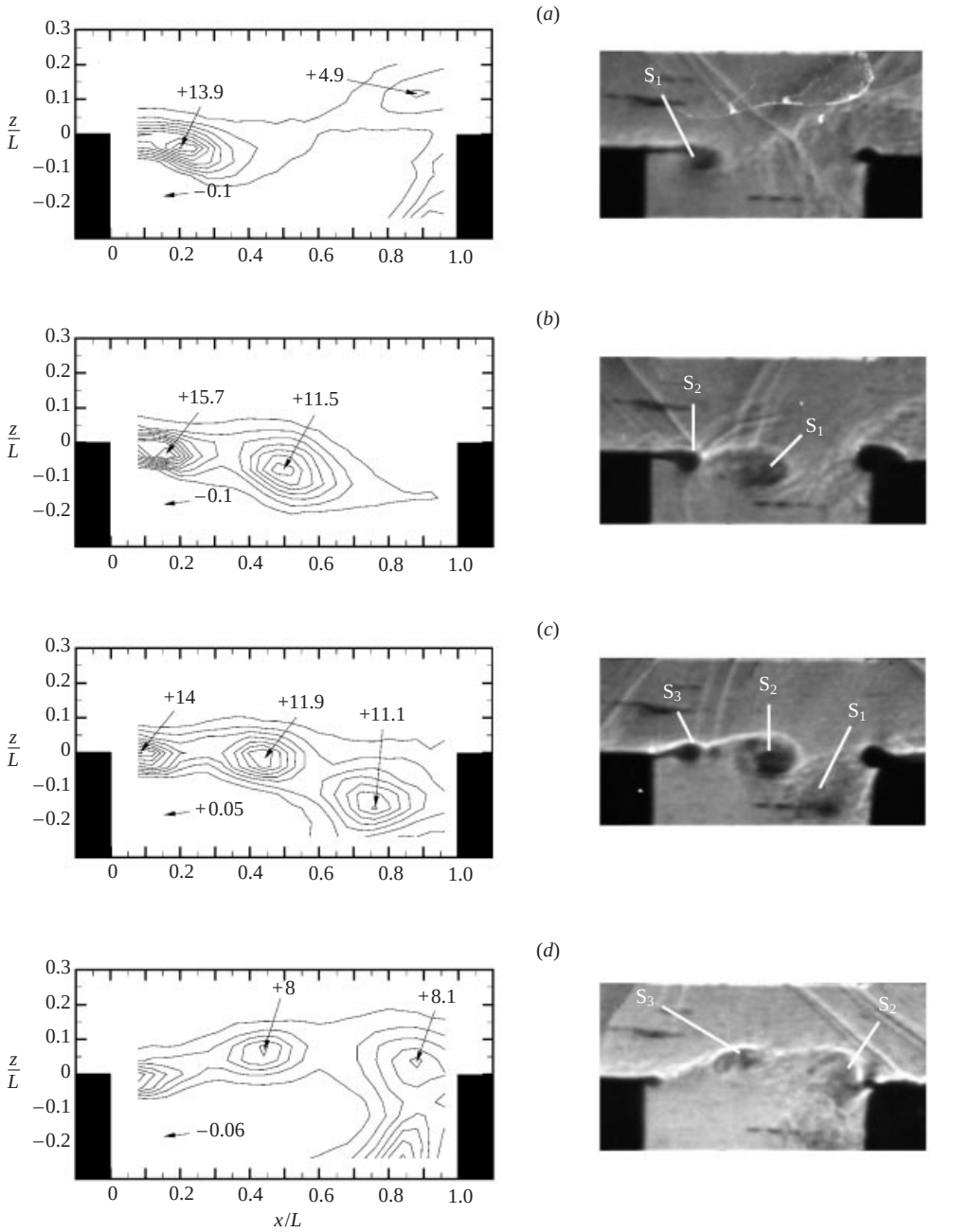

FIGURE 12. Contour plot of $\langle \Omega_y \rangle L/U_e$: (*a*) phase 10, (*b*) phase 15, (*c*) phase 20, (*d*) phase 5. Corresponding schlieren pictures are shown on the right.

As noticed above (see § 3.2), despite integration of the schlieren technique, the pictures reveal well-defined two-dimensional structures. This is confirmed by measurements performed in the (x, y)-plane coinciding with the open face of the cavity, see figure 7(*b*). Iso-level values of $-\partial\langle W \rangle/\partial x$ measured in this plane for phase 17 are plotted in figure 15(*a*), figure 15(*b*) showing the corresponding spanwise vorticity

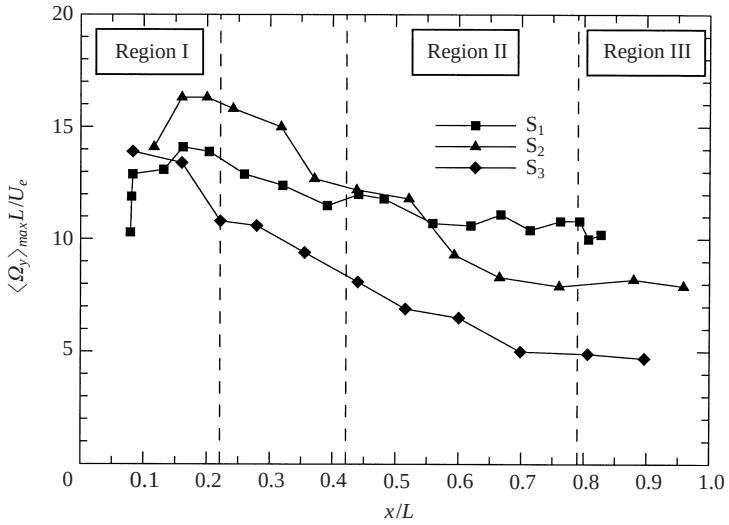

FIGURE 13. Variation of the spanwise vorticity peak values.

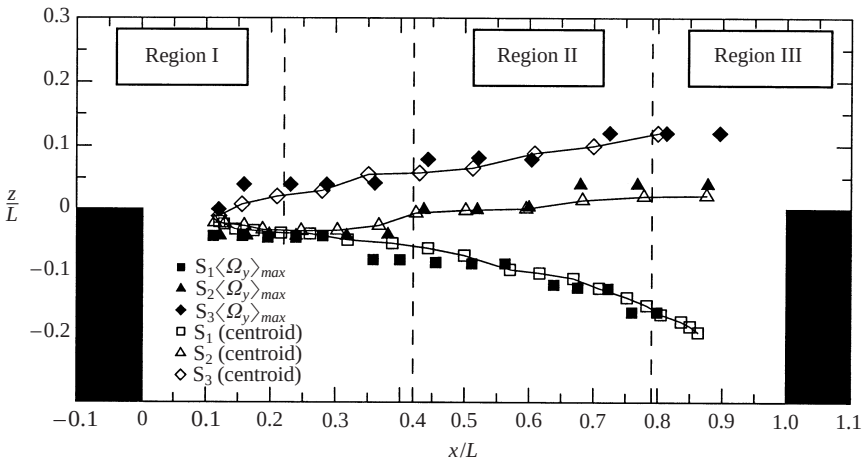

FIGURE 14. Loci of the vorticity centroids and vorticity peaks.

$\langle\Omega_y\rangle$. The other phases show similar strong evidence that the coherent vortices in this flow are two-dimensional. Note that in figure 15(a), the top and bottom limits ($y/L = \pm 1.2$) correspond to the side windows of the tunnel where boundary layers develop. The latter have not been explored, but it is remarkable that their presence only weakly affects the two-dimensional character of the mixing layer vorticity. The two-dimensional nature of the flow is weakened at the end of region III where the mixing layer is subjected to a strong interaction with the downstream cavity edge. This is illustrated in figure 16 which shows the phase variation of the vertical velocity, $\langle W\rangle$, at three spanwise positions close to the edge. The mass inflow/outflow process is clearly evidenced by alternation of positive and negative values of the velocity. Differences in $\langle W\rangle$ occur especially during phases 5 to 12, which correspond to the ejection of fluid from the cavity. However, even during this interaction process, the three-dimensional effects remain weak.

The present flow should differ from shallower cavity flows through a stronger two-dimensional organization, as characterized above. This was confirmed by comparisons

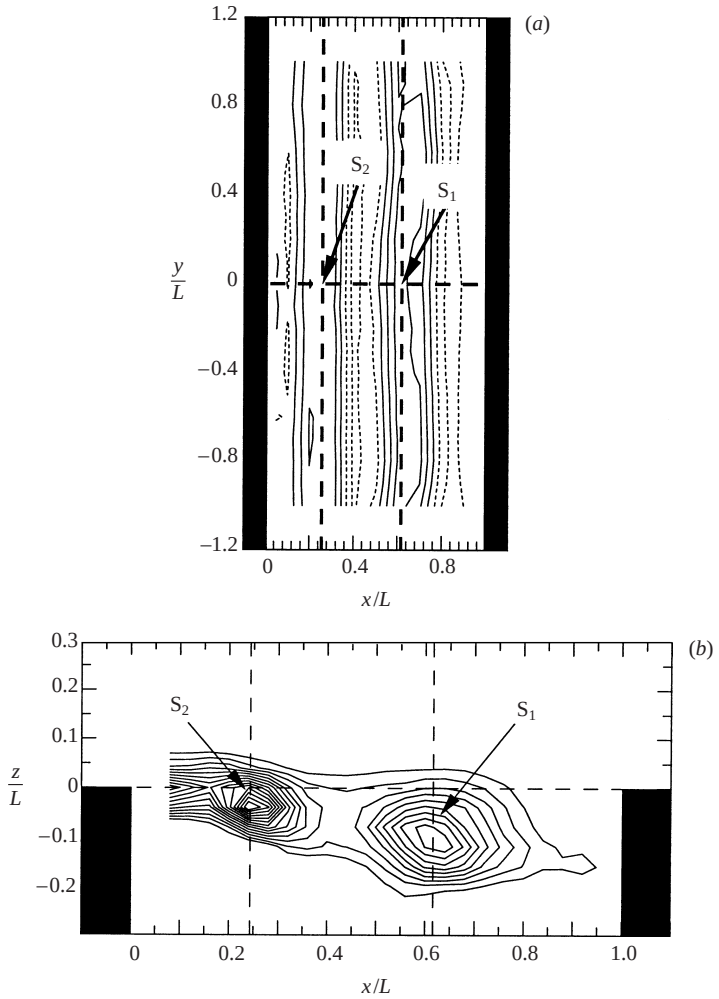

FIGURE 15. Phase 17: (*a*) iso-levels of $-\partial\langle W\rangle/\partial x$ in the horizontal plane $z = 0$, (*b*) contour plots of the phase-averaged spanwise vorticity $\langle\Omega_y\rangle$ in the vertical symmetry plane.

with results obtained with a cavity of aspect ratio $L/D = 2$ (Forestier *et al.* 2000). In such a cavity, the flapping of the mixing layer was reduced and the conditional statistics in the horizontal plane showed clear three-dimensional distortions compared with figure 15(*a*). A more efficient coupling between the cavity acoustics and the shear layer is expected when the aspect ratio L/D is reduced. An explanation could be that a smaller part of the cavity acoustics is radiated outward when the depth of the cavity is increased.

3.5. *Kinematics*

In this section, our conditional results are discussed in the light of those obtained in other forced and unforced mixing layers. Figure 17 shows the longitudinal position of the centroids, x_c, against the non-dimensional time tU_e/L. Convection velocities may be calculated by differentiation of these data. The results, obtained using a second-order discretization, are plotted against x_c and against time in figures 18(*a*) and 18(*b*), respectively. The dashed lines in figure 18(*a*) correspond to the three regions

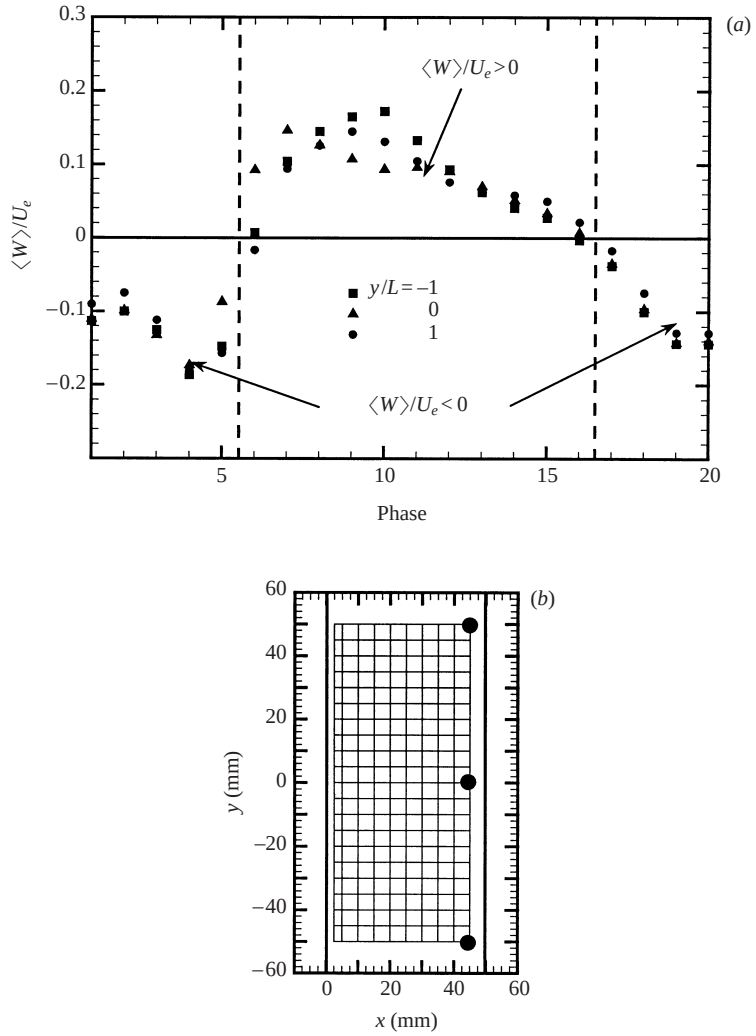

FIGURE 16. Vertical component of the phase-averaged velocity measured at three locations, $x/L = 0.9$, $y = -L, 0, L$ and $z = 0$, as sketched in (b).

of the flow defined in § 3.3. In region I, which corresponds to the largest spreading rate ($\mathrm{d}\theta/\mathrm{d}x = 0.12$), the convection velocities grow linearly from 0 to $0.5U_e$. In the relaxation region, the convection velocities remain almost constant except that of the ejected structure S_3. At the beginning of region II, the values obtained are close to 0.5. In region III, the convection velocities of structures S_2 and S_3 increase up to $0.75U_e$ whereas structure S_1 decelerates while it is trapped into the cavity.

The mean convection velocity of S_2, the structure which interacts directly with the downstream corner, see figure 2, is found to be $U_{c2}/U_e \approx 0.5$ (here U_{c2} denotes the average over a period of the velocity of this structure). This particular value has been used in the definition of a modified set of Rossiter's parameters used in § 3.1, see figure 6. It is similar to that found by Hussain & Zaman (1985) in the self-preserving region of a turbulent plane mixing layer, where a standard spreading rate $\mathrm{d}\theta/\mathrm{d}x = 0.035$ was observed. It is striking that a similar convection speed and spreading rate are obtained in the present flow (region II), which is strongly out of equilibrium.

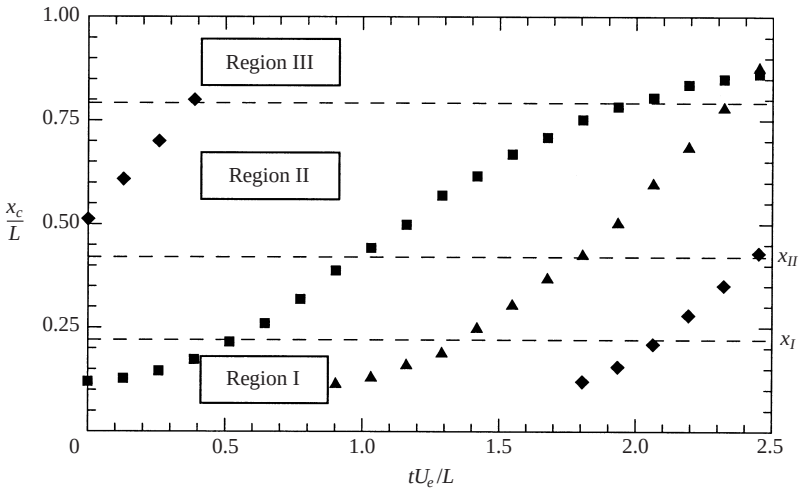

FIGURE 17. Vorticity centroid position versus time: structure S_1 (square), S_2 (triangle), S_3 (diamond). The time origin is arbitrary.

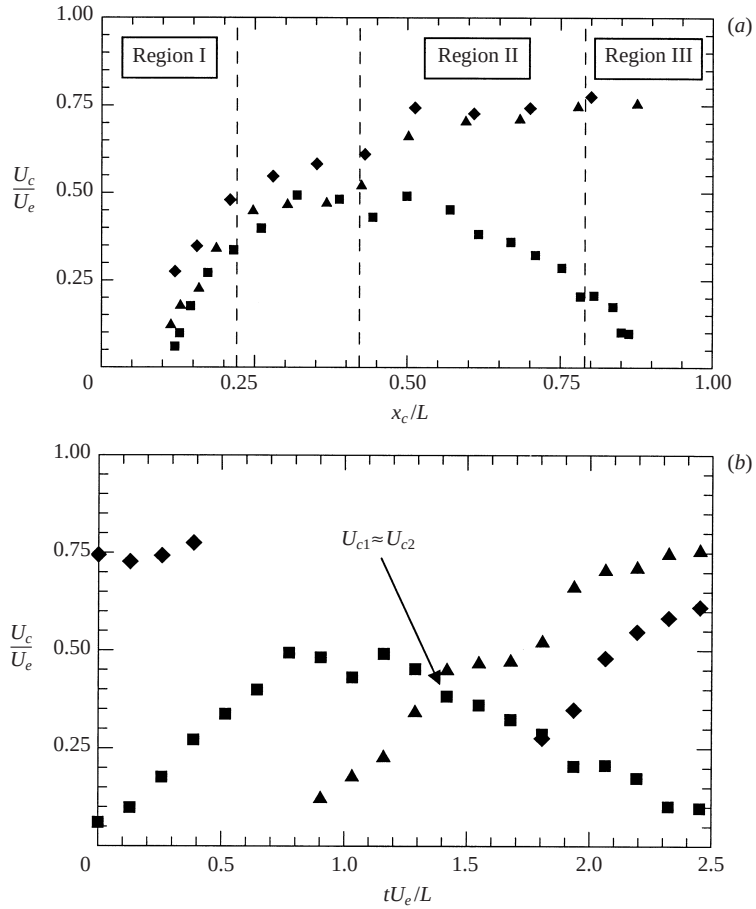

FIGURE 18. (*a*) Streamwise evolution of the vorticity centroid convection velocity and (*b*) convection velocities versus time: structure S_1 (square), S_2 (triangle), S_3 (diamond). The time origin is arbitrary.

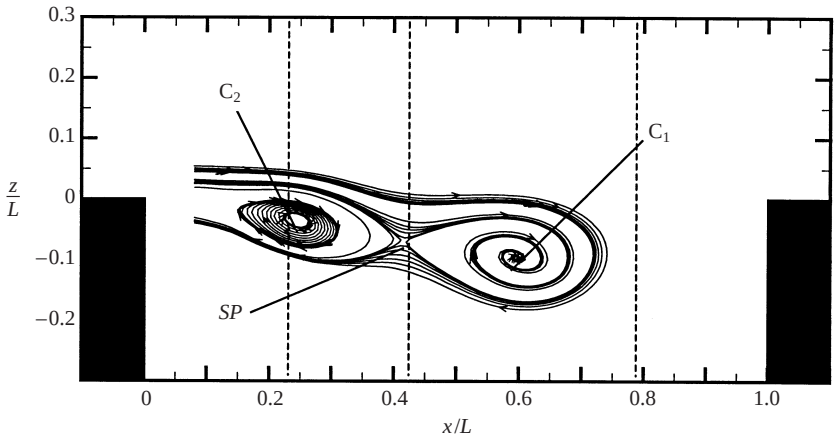

FIGURE 19. Pseudo-streamlines of phase 17 in a frame convected at velocity $U_{c1} = U_{c2}$ (see figure 18*b*) showing the centres C_1, C_2 of structures S_1, S_2 and the saddle point *SP*.

As proposed by Cantwell & Coles (1983), the kinematics of coherent structures may be described in terms of the formation and evolution of saddle points between vortices. Saddle points must be defined in a reference frame moving at the same speed as the coherent structures. Figure 18(*b*) shows that each coherent structure possesses its own convection velocity. As seen on this figure, the convection velocities of structures S_1 and S_2 become identical at the particular time $tU_e/L = 1.4$. This corresponds to phase 17, which has already been characterized through its vorticity field in figure 15(*b*). The pseudo-streamlines in a frame moving at this convection velocity are sketched in figure 19 (these streamlines have been obtained using the Tecplot™ streamline routine without any further post-processing). We have indicated the points C_1 and C_2 which correspond to the position of the centres of structures S_1 and S_2 and the point *SP* which corresponds to the saddle point. The spiral shape of the streamlines of structure S_1 may denote three-dimensional effects. This figure will be used below to discuss phase-averaged results.

3.6. *Energetics*

A thorough characterization of the phase-averaged statistics has been made and is available for CFD validation purposes.

As explained in § 2.4, the velocity fluctuations may be split into coherent and random contributions ($u_0' = \tilde{u} + u'$). The following kinetic energies are considered first:

$$k_0 = (\overline{u_0'^2} + \overline{w_0'^2})/2, \quad \overline{\tilde{k}} = (\overline{\tilde{u}^2} + \overline{\tilde{w}^2})/2, \quad \bar{k} = (\overline{\langle u'^2 \rangle} + \overline{\langle w'^2 \rangle})/2.$$

The first expression is based on the standard Reynolds average. The others two correspond to ensemble averages over the 20 phases. (The standard Reynolds average is given by $k_0 = \overline{\tilde{k}} + \bar{k}$.)

Figure 20 shows profiles of k_0/U_e^2, $\overline{\tilde{k}}/U_e^2$, $\bar{k}/U_e^2$. The periodic component, $\overline{\tilde{k}}/U_e^2$, is dominant up to a distance of $x/L = 0.8$ where it becomes comparable to the random component, $\bar{k}$. The peak values of the coherent component amount to nearly 60–70% of the maximum total energy. A shift of these peaks in the lower part of the mixing layer can be observed when approaching the downstream wall. Profiles of the corresponding shear stresses are shown in figure 21. Apart from in region III, the shear stress is dominated by the periodic motion. The peak values are found to be $\overline{\tilde{u}\tilde{w}}/\overline{u_0'w_0'} \approx 0.6$–$0.7$.

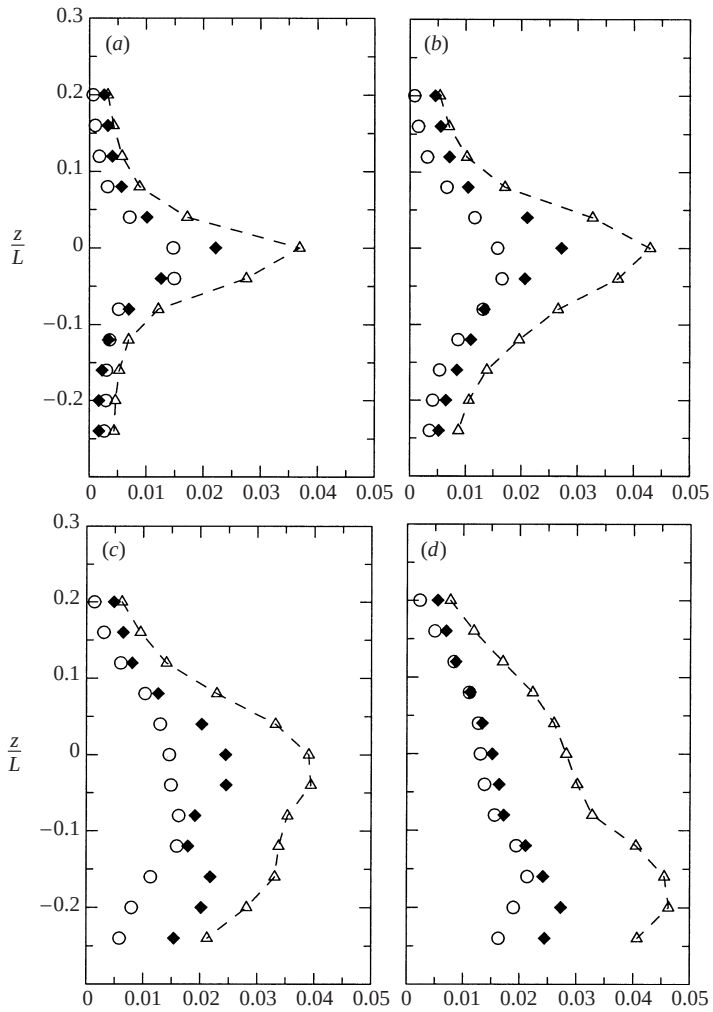

FIGURE 20. Profiles of mean total kinetic energy, k_0/U_e^2 (- - -△- - -), periodic kinetic energy, $\overline{\tilde{k}}/U_e^2$ (◆), and random kinetic energy, $\overline{\langle k \rangle}/U_e^2$ (○), at $y = 0$ and (*a*) $x/L = 0.2$, (*b*) 0.4, (*c*) 0.6, (*d*) 0.8.

Figure 22 shows the spatial distribution of the phase-averaged stresses, $\tilde{u}^2$, $\tilde{w}^2$ and $-\tilde{u}\tilde{w}$ of the cyclic motion of phase 17 (see figures 15 and 19). The contour shapes are in agreement with the topology of the flow shown in figure 19. In particular, the shear stress $-\tilde{u}\tilde{w}$ associated with structure S_1 exhibits a clear quadripolar or 'cloverleaf' distribution typical of a monopolar vortex. Contour levels of the phase-averaged shear stress of the random fluctuations, $\langle u_i' u_j' \rangle$, are shown in figure 23. These quantities are weaker than their coherent counterpart (compare with figure 22), in accordance with the results of figure 21. However, it must be noted that $\langle u_i' u_j' \rangle$ may be larger than the corresponding standard Reynolds stresses. In the present case, the peak value of $\langle u'^2 \rangle / U_e^2$ of phase 17 exceeds $\overline{u_0'^2}/U_e^2$ by as much as 30%.

Now, as mentioned in the introduction, the distribution of $\langle u_i' u_j' \rangle$ in the flow field is an important problem to be discussed since it gives insights into the small-scale production mechanisms related to coherent structures. Compared with figure 19, figure 23(*a*, *b*) shows that the maxima of $\langle u'^2 \rangle / U_e^2$ and $\langle w'^2 \rangle / U_e^2$ coincide with the vortex centres C_1 and C_2. This is also found in the whole body of experimental results

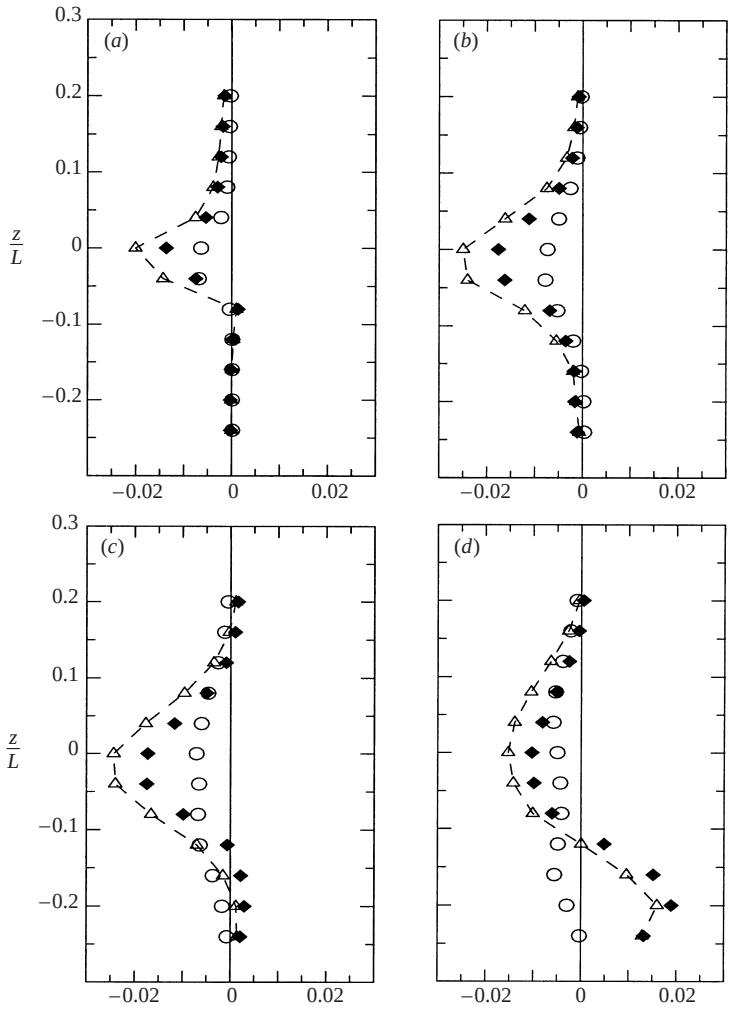

FIGURE 21. Profiles of mean shear stress, $\overline{u_0'w_0'}/U_e^2$ (- - -△- - -), periodic shear stress, $\overline{\tilde{u}\tilde{w}}/U_e^2$ (◆), and random shear stress, $\overline{\langle u'w'\rangle}/U_e^2$ (○), at $y = 0$ and (*a*) $x/L = 0.2$, (*b*) 0.4, (*c*) 0.6, (*d*) 0.8 (for symbols see above).

on mixing layers and is a common feature of these flows. Differences appear when considering the shear stress $-\langle u'w'\rangle$. The present results, see figure 23(*c*), indicate that $-\langle u'w'\rangle/U_e^2$ is maximum in the centres, where it is 3 to 4 times larger than in the saddle region. Similar observations have been made by Lyn *et al.* (1995) in the base region of their square cylinder. But this departs from mixing layer results where $-\langle u'w'\rangle$ is found to reach its maximum in the saddle regions. In figure 24, the iso-values of $-\langle u'w'\rangle$ are plotted together with those of $\langle\Omega_y\rangle$, of the squared phase-averaged two-dimensional rate of strain $\langle S\rangle^2 = \langle \boldsymbol{d}\rangle : {}^t\langle \boldsymbol{d}\rangle$ (with $\boldsymbol{d} = (\boldsymbol{\nabla u} + {}^t\boldsymbol{\nabla u})/2$) and of the phase-averaged second invariant $\langle Q\rangle$ of $\langle \boldsymbol{\nabla u}\rangle$ (Jeong & Hussain 1995). These results are very similar to those obtained in mixing layers, see e.g. Hussain (1986), except for the shear stress.

Coupling between small-scale turbulence and coherent strain fields may also be characterized from the phase-averaged production terms of the random kinetic energy $\langle k\rangle$. These terms comprise the contributions of the normal and shear stresses, which

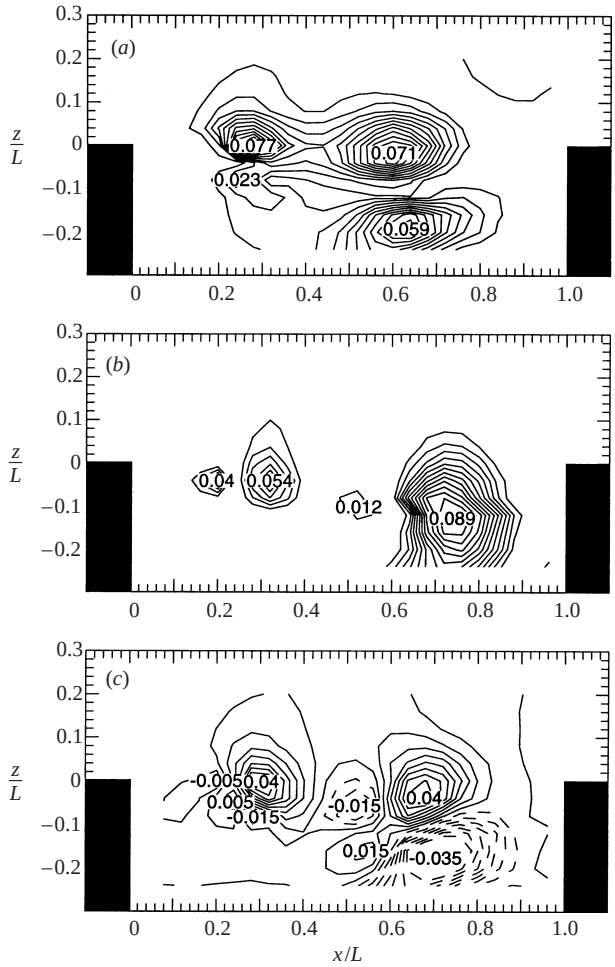

FIGURE 22. Phase 17: contour plots of (*a*) $\tilde{u}^2/U_e^2$ (levels from 0.005 to 0.077 in increments of 0.006), (*b*) $\tilde{w}^2/U_e^2$ (levels from 0.012 to 0.089 in increments of 0.007), (*c*) $-\tilde{u}\tilde{w}/U_e^2$ (levels from −0.035 to 0.04 in increments of 0.005). Negative values shown as dashed lines.

are labelled $\langle P_n \rangle$ and $\langle P_s \rangle$ respectively (see Lyn *et al.* 1995):

$$\left.\begin{aligned} \langle P_n \rangle &= -\langle u'^2 \rangle \frac{\partial \langle U \rangle}{\partial x} - \langle w'^2 \rangle \frac{\partial \langle W \rangle}{\partial z}, \\ \langle P_s \rangle &= -\langle u'w' \rangle \left(\frac{\partial \langle U \rangle}{\partial z} + \frac{\partial \langle W \rangle}{\partial x} \right). \end{aligned} \right\} \tag{8}$$

Contours of $\langle P_n \rangle L/U_e^3$, $\langle P_s \rangle L/U_e^3$ and $\langle P \rangle L/U_e^3$, with $\langle P \rangle = \langle P_n \rangle + \langle P_s \rangle$ are shown for phase 17 in figures 25(*a–c*). $\langle P \rangle L/U_e^3$ is essentially positive and is maximum in the centres of the vortices. It is observed that most of the contribution to $\langle P \rangle$ comes from $\langle P_s \rangle$.

A consensual picture established from mixing layer studies is that small-scale perturbations are mainly produced by the vortex stretching which takes place in the saddle regions between two adjacent spanwise structures. Shear stress $-\langle u'w' \rangle$ and associated production are then expected to be maximum here. On the other hand,

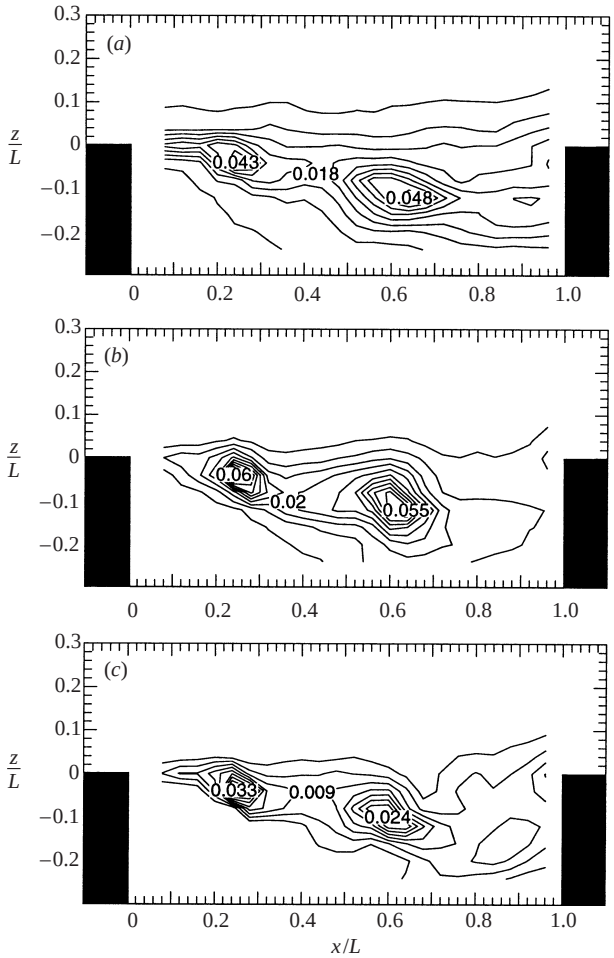

FIGURE 23. Phase 17: contour plots of (*a*) $\langle u'^2\rangle/U_e^2$ (levels from 0.003 to 0.048 in increments of 0.005), (*b*) $\langle w'^2\rangle/U_e^2$ (levels from 0.005 to 0.06 in increments of 0.005), (*c*) $\langle -u'w'\rangle/U_e^2$ (levels from 0.003 to 0.033 in increments of 0.003).

the presence of energetic perturbations in the coherent structures is attributed to a meandering of the vortices and possibly to transport of turbulence from the saddle regions. Our results conflict this scenario. This difference may possibly be related to the particularly strong two-dimensional character of the flow, which could enable the observation of mechanisms here which are usually hidden by a rapid onset of three-dimensionality in typical free mixing layers. This problem will be discussed further in § 4.2.

3.7. *Vortex/edge interaction*

An effort has been made to further describe the region where the vortices interact with the cavity wall. A Kulite™ sensor was placed below the downstream edge of the cavity, at $x = 50\,\text{mm}$, $y = 0$, $z = -1\,\text{mm}$. We have explored the phase relation between this signal and that delivered by the central sensor located on the upstream vertical wall ($x = 0$, $y = 0$, $z = -35\,\text{mm}$). The two pressure signals, low-pass filtered at 3 kHz by means of a digital filter, are shown in figure 26 for a typical run. They

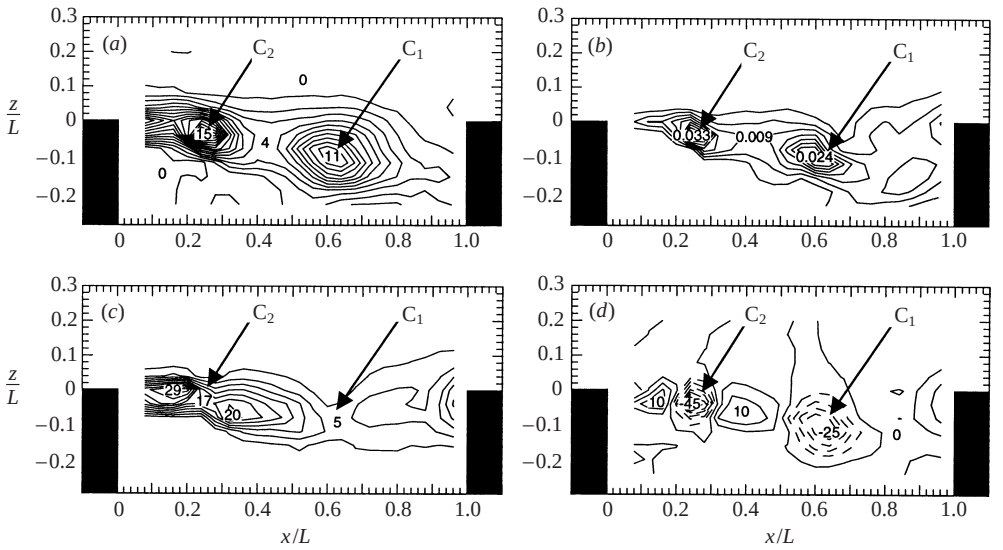

FIGURE 24. Phase 17: contour plots of (*a*) the phase-averaged vorticity $\langle \Omega_y \rangle L/U_e$, (*b*) the shear stress $\langle u'w' \rangle / U_e^2$, (*c*) the strain rate $\langle S \rangle^2 L^2/U_e^2$, and (*d*) the second invariant of $\langle \nabla \boldsymbol{u} \rangle$, $\langle Q \rangle L^2/U_e^2$. The centres C_1 and C_2 of the structures S_1 and S_2 are indicated.

are labelled P_1 and P_2. The peak-to-peak amplitude of P_2 is almost twice that of P_1. Note that P_2 is subjected to larger modulations than P_1. This denotes a loss of flow coherence in this region due to the violent breaking of the shear layer. Consequently, 'jitter' affects the conditional results in this region (see Appendix B for a detailed discussion about jitter).

A detailed study of this region would have necessitated a more local eduction scheme than that based on P_1. However, the conditional analysis of P_2 using P_1 as a phase reference gives interesting insight into some features of the flow/acoustic interaction. Distribution of the phase-averaged downstream pressure $\langle P_2 \rangle$ and corresponding iso-levels of $\langle \Omega_y \rangle$ are shown in figure 27(*b*) at different phases of the vortex/corner interaction. The region covered by the figures corresponds to the end of region II and region III as defined in § 3.3. A positive peak pressure, corresponding to phase 2, occurs when the first structure S_1 dives down the vertical wall (see figure 12): external high-speed fluid is convected downward and contributes to a rise of the total pressure. The phase-averaged transverse velocity component $\langle W \rangle$ at $z = 0$ shows that this phase of the flow cycle corresponds to strongly negative values of $\langle W \rangle$ at the back of the structure. As the following structure, S_2, impinges on the downstream edge of the cavity, see phase 6, a negative peak occurs which approximately coincides with the impingement of S_2 on the edge. This sharp pressure minimum is related to the total pressure loss in the viscous core of the vortex. When the structure S_3 is swept above the cavity edge, see phase 11, $\langle P_2 \rangle$ in figure 27(*a*) exhibits an inflection point. From detailed inspection of the flow visualizations, we have observed that this event coincides with the emission of a wave front. Then, $\langle P_2 \rangle$ remains approximately constant before a new structure S_1 reaches the downstream cavity wall (see phase 16). Similar behaviour has been observed in a vortex/edge interaction at low Reynolds number, see e.g. Tang & Rockwell (1983).

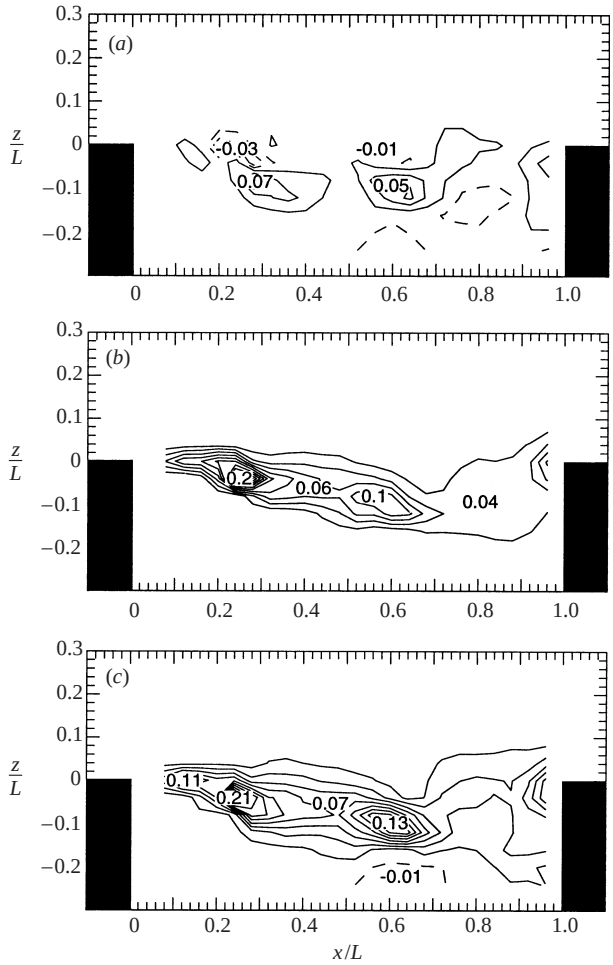

FIGURE 25. Production of random fluctuations for phase 17: (*a*) $\langle P_n \rangle L/U_e^3$ (levels: -0.05 to 0.07 in increments of 0.02), (*b*) $\langle P_s \rangle L/U_e^3$ (levels: 0.02 to 0.2 in increments of 0.02), (*c*) $\langle P \rangle L/U_e^3$ (levels: -0.01 to 0.21 in increments of 0.02). See text for the definitions.

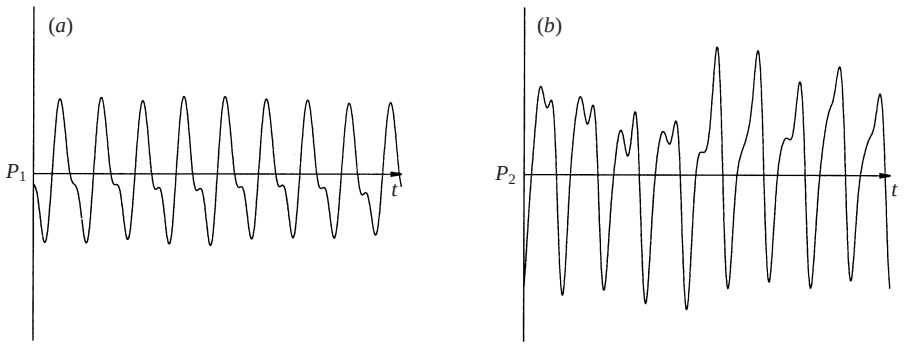

FIGURE 26. Low-pass filtered pressure signal delivered by transducers located in (*a*) the upstream wall, $x = 0$, $y = 0$, $z = -35$ mm, (*b*) the downstream wall, $x = 50$ mm, $y = 0$, $z = -1$ mm (same scales).

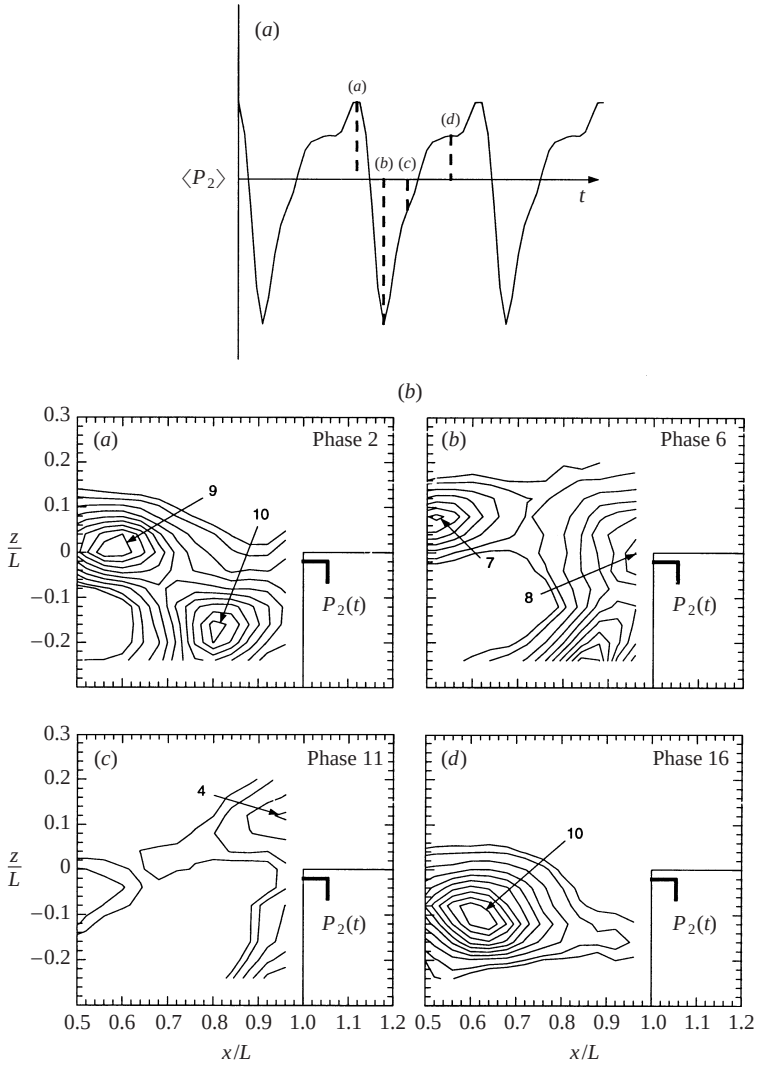

FIGURE 27. (*a*) Phase-averaged downstream edge pressure $\langle P_2 \rangle$ and (*b*) contour plots of the phase-averaged vorticity $\langle \Omega_y \rangle L/U_e$ for phase 2, 6, 11 and 16 (*a–d*).

4. Discussion

Two interesting features described in § 3 are the coherent structure formation process and small-scale production in the core regions. These two mechanisms are further discussed in this section.

4.1. *Formation of the coherent structures*

Refined measurements have been performed in region I in order to check the hypothesis of a 'collective interaction mechanism', see § 3.3. The longitudinal extent of the measurement region was $1\,\text{mm} \leqslant x \leqslant 7\,\text{mm}$, which corresponds to nearly half region I: $x/\theta_0 \leqslant 10$ ($x/L \leqslant 0.12$). Its vertical extent was $-2.5\,\text{mm} \leqslant z \leqslant 0$, that is $-4 \leqslant z/\theta_0 \leqslant 0$. The mesh size was set as small as $\Delta x = \Delta z = 0.25\,\text{mm}$, which is nearly the characteristic size of the LDV measurement volume.

A typical result of the conditional analysis of these refined data is given in figure 28

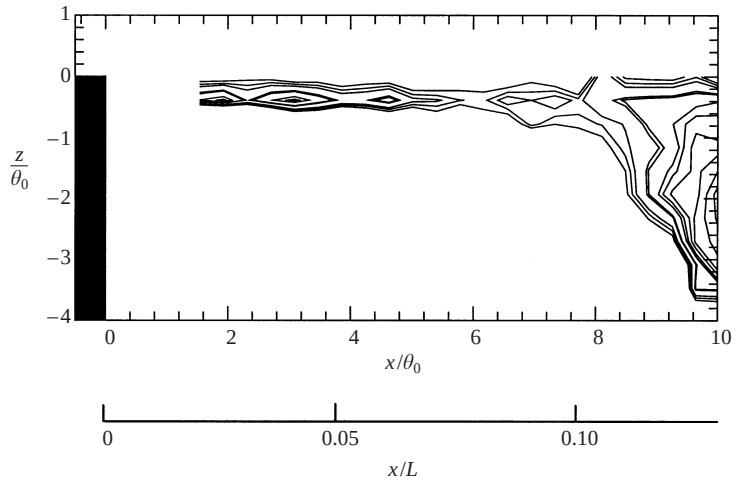

FIGURE 28. Phase 9: refined measurements in region I of phase-averaged random kinetic energy $\langle k \rangle$.

which shows contours of $\langle k \rangle$ at phase 9. It is remarkable to note how thin the vorticity layer is in this region. Its thickness is of the order of θ_0. However, the contour plots do not reveal any clear tendency to spatial organization. In fact, the results of figure 28 only show that the initial flow organization, if any, does not lock onto the fundamental frequency of the cavity. Note that Ho & Nosseir (1981) have already suggested that the individual vortices, which result from Kelvin–Helmholtz instabilities, do not keep a well-defined phase relation during the 'collective interaction'. Detailed inspection of schlieren pictures, such as those shown in figure 2, has revealed the presence of small and highly concentrated vortices in the region of the upstream cavity edge, but their position was observed to be randomly distributed. The amalgamation process of such eddies escapes the present conditional analysis and characterization of a spatial organization within region I would have necessitated a completely different eduction scheme.

Consequently, the relevance of the 'collective interaction' to describe the vortex formation process is not confirmed. The only evidence for this hypothesis remains that (i) the shear layer is strongly forced at a frequency lower than the fundamental frequency of the shear layer and (ii) the spreading rate is very high.

We have favoured up to now the assumption that the shear layer could be described almost in isolation, as a free shear layer. As discussed by Colonius (2001) and by Rowley, Colonius & Basu (2002), an alternative to this 'shear layer' regime of the flow is to consider the flow in a more global sense, accounting for non-parallel effects and for coupling with the flow inside the cavity. This alternative is supported by the observations made by Gharib & Roshko (1987) of a 'wake-mode' regime which was found to replace the 'shear layer' regime when the ratio between their cavity length and the initial momentum thickness was large enough. Following Gharib & Roshko (1987) and Rowley *et al.* (2002), the 'wake mode' is characterized by higher pressure oscillations, by the formation of a shed vortex whose dimension is close to that of the cavity size and by free-stream fluid impinging on the cavity base. Such behaviour is not observed in the present experiment. The transition between the 'shear layer mode' and the 'wake mode' depends on the ratio L/θ_0 (Gharib & Roshko 1987) and also on the Mach and Reynolds numbers (Rowley *et al.* 2002). In the present flow, $L/\theta_0 \approx 80$, see figure 9, a value which is half that observed for a transition

between the 'shear mode' and the 'wake mode' in the incompressible flow of Gharib & Roshko (1987). It is interesting to note that $L/\theta_0 \approx 80$ exactly corresponds to the lower limit below which the cavity oscillations were completely suppressed in their experiment. This confirms that the physics of the flow depends substantially on the Mach number and on the Reynolds number. The DNS results of Rowley *et al.* (2002) on compressible cavity flows show that the transition to the 'wake mode' occurs when the cavity aspect ratio increases beyond approximately $L/D = 4$, and for large enough values of L/θ_0 and D/θ_0. This is not relevant for our deep cavity case. Finally, the 'wake mode' suggests the existence of global unstable modes in the cavity, as in the near-field behind a bluff body. Such a global instability should develop after the shear layer becomes absolutely unstable, a mechanism which could provide the feedback mechanism leading to the wake mode (Rowley *et al.* 2002). This could occur when a strong enough recirculating flow develops inside the cavity. However, inspection of our phase-averaged velocity results shows that this does not occur in the present shear layer, the latter never being absolutely unstable in the sense of Huerre & Monkewitz (1985). The conclusion is that the present flow is not subjected to a 'wake mode' regime.

However, global effects are brought to mind when looking at the frames of figure 2. One may note in particular the flapping of the initial portion of the shear layer, in region I, during phases 1 to 5. During these phases, structure S_1 is captured by the cavity and comes closer to structure S_2, as if both structures were merging. The concentration of vorticity that results from this mechanism seems responsible for the flapping of region I, through a Biot-Savart induction effect. Under this circumstance, impingement of the large vortical structures on the downstream corner influences the sensitive region of the shear layer close to the upstream corner. Consequently, the shear layer cannot be considered as a free shear layer. To what extend this non-local effect influences the formation of the vortices remains unknown. This could be one of the components of the 'collective interaction'.

To end on that point we may repeat, following Gharib & Roshko (1987), that the development of the initial portion of the shear layer over the cavity may be similar to that of a free shear layer but modulated by a low-mode cavity wave and exhibiting an enhanced growth rate and possibly the 'collective interactions' described by Ho & Huang (1982) and Oster & Wygnanski (1982).

4.2. *Small-scale production and coherent structures: the elliptic instability?*

As discussed above, a distinctive characteristic of the present flow is the concentration of 'incoherent' shear stress in the structure centres. This could be due to measurement limitations, namely coherent structure jitter or bias due to particle inertia. We show in Appendix B that jitter contributes to less than 10% of the random perturbations. Moreover, we also show that jitter, whatever its level, cannot explain the present distribution of the random shear stress. We also show in Appendix C that particle bias is negligible.

A possible physical mechanism that could promote the production of small-scale perturbations in the vortex centres of our flow is the elliptic instability which occurs in elliptically shaped streamlines of two-dimensional flows, see Pierrehumbert (1986), Bayly (1988), Moore & Saffman (1975), Waleffe (1990). The role of these instabilities in the coherent structures of a mixing layer was first studied by Pierrehumbert & Widnall (1982) who identified the existence of a broadband spectrum of three-dimensional instabilities, most visible in the central region of the vortices. Elliptic instabilities result from the stretching of vorticity perturbations by a strain field

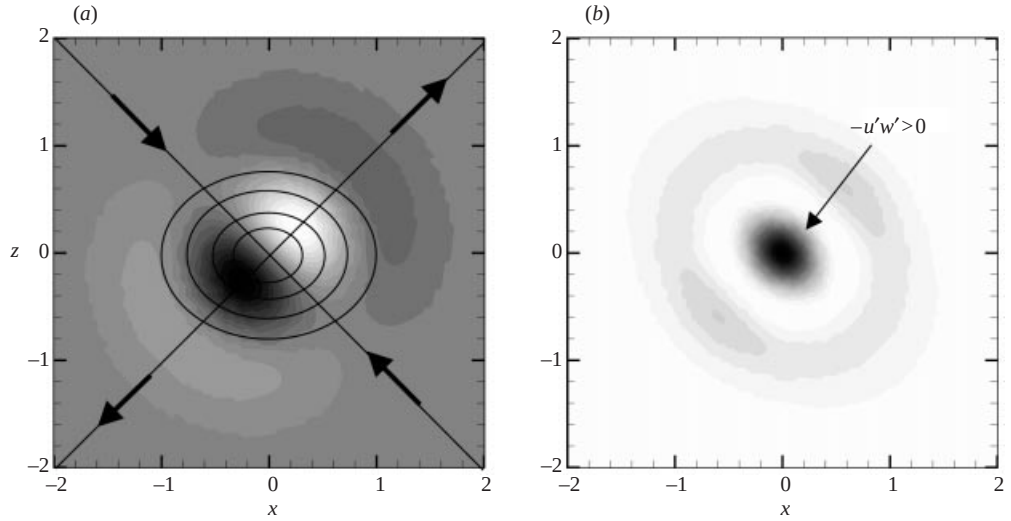

FIGURE 29. Elliptic instability in a Lamb–Oseen vortex, see equation (9), subjected to a 45° strain: (*a*) fluctuation of the spanwise vorticity $\omega_y'(x,z,t)$ of the most amplified mode (arbitrary levels), (*b*) shear stress $-u'w'(x,z,t)$ (arbitrary levels).

whose rate is proportional to the ellipticity of the streamline. In an array of vortices, the strain is induced on a given vortex by the neighbouring vortices. In this case, the elliptic instability amounts to a cooperative instability mechanism which results from triadic resonance between two inertial waves and the strain, see Moore & Saffman (1975). These instabilities have been shown to provoke the merger of two co-rotating vortices in the absence of perturbations in between the vortices, see Meunier & Leweke (2000). Consequently, two different linear mechanisms participate in the onset of three-dimensionality in a mixing layer, namely the development of elliptic instabilities in the vortex cores and the amplification of longitudinal vorticity through stretching in the hyperbolic regions – or saddles. Our conjecture is that, in this strong two-dimensional flow, the core instabilities are stronger than the hyperbolic instabilities.

One must show however that an elliptic instability leads effectively to concentration of the shear stress within the vortex core. We will prove this statement by considering the shear stress of a perturbation field corresponding to the elliptic instability which develops within a vortex subjected to a small strain. The vortex is modelled by a Gaussian vorticity distribution:

$$\langle \Omega_y \rangle(x,z) = \exp\{-(x^2+z^2)\}. \tag{9}$$

This corresponds to a Lamb–Oseen vortex with a unit radius and circulation $\Gamma = 2\pi$. A strain field of rate ε, oriented at 45°, is superposed on this flow. The resulting deformation rate tensor is

$$\nabla \boldsymbol{u} = \begin{pmatrix} 0 & \varepsilon+\gamma \\ \varepsilon-\gamma & 0 \end{pmatrix}, \tag{10}$$

where $\gamma(x,z) = \langle \Omega_y \rangle(x,z)/2$ denotes the rotation rate of the vortex. Figure 29 shows the structure of the most-amplified mode obtained from the linearized Euler equations in the asymptotic limit of a weak strain rate $\varepsilon \ll 1$. Figure 29(*a*) shows the spanwise vorticity perturbation field ω_y' (note the similarity between this figure and figure 9 of

Pierrehumbert & Widnall 1982). This perturbation grows with the characteristic time scale $\tau_{elliptic} = C/\varepsilon$, where C is a constant close to 0.5 ($C = 9/16$ in the asymptotic limit $\varepsilon/\gamma \to 0$), and it exhibits a dipolar structure which is characteristic of such an instability (see Waleffe 1990; Sipp, Coppens & Jacquin 1999).

The corresponding iso-values of $-u'w'$ are plotted in figure 29(b). They look like those obtained in the experiment in the sense that the product $-u'w'$ is positive and the maximum is located at the vortex centre. This shows that the elliptic instability could contribute to a distribution of the shear stress localized in the vortex centre, as in the present experiment.

It must also now be checked, that the instability has time to develop while the structures are convected over the cavity. Let us consider, first, the time scale of the instability, $\tau_{elliptic} = C/\varepsilon$, with $C \approx 0.5$. The strain rate ε may be evaluated by considering the phase-averaged strain rate $\langle S \rangle$ plotted in figure 24(c). In the centre C_2 of structure S_2 $\varepsilon^2 L^2/U_e^2 \approx 17$. This gives $\varepsilon \approx 21$ kHz. An alternative is to determine ε from the rotation rate $\gamma \approx \langle \Omega_y \rangle_{max}/2$ and the structure ellipticity, i.e. $E \approx \sqrt{(\gamma + \varepsilon)/(\gamma - \varepsilon)}$. Inspection of structure S_2 which comes from region I, see figures 15 and 19, shows that it is elliptical with an aspect ratio (ratio between major and minor axes) $E \approx 2$. This gives $\varepsilon/\gamma \approx 3/5$. The rotation rate γ may be evaluated as $\gamma \approx \langle \Omega_y \rangle_{max}/2$ with $\langle \Omega_y \rangle_{max} L/U_e \approx 15$, as seen in figure 24($a$), for structure S_2 at the end of region I. This leads to $\varepsilon \approx 3\gamma/5 \approx 23$ kHz, close to the value found above. These estimations must be however corrected for the effect of the mesh size, on which the exact values of $\langle \Omega_y \rangle$ and $\langle S \rangle$ depend. The values found above are minima. Tests have shown that correction by a factor of 2 is a reasonable choice. Applying this factor to ε leads finally to $\varepsilon \approx 40$ kHz. Finally, an estimation of the time scale of the instability is $\tau_{elliptic} \approx 1/(0.5\varepsilon) \approx 50\,\mu$s.

This time scale must be compared now to a convection time scale. The time it takes for a structure S to reach a downstream position x is

$$\tau_c^S(x) \equiv \int_0^x \frac{\mathrm{d}x}{U_c^S(x)},$$

where $U_c^S(x)$ denotes the convection velocity of the structure. This time scale may be deduced from figure 17. Considering the two characteristic distances x_I and x_{II} indicated on that figure which correspond to the downstream and upstream limits of regions I and II, respectively, figure 17 shows the times structure S_1 takes to cover these distances starting from their origin are $\tau_c^S(x_I)U_e/L \approx 0.5$ and $\tau_c^S(x_{II})U_e/L \approx 1.1$. The same values are obtained for structure S_2. This leads to the following characteristic time scales: $\tau_c^S(x_I) \approx 100\,\mu$s and $\tau_c^S(x_{II}) \approx 210\,\mu$s.

Consequently, $\tau_c^S(x_I)/\tau_{elliptic}(x_I) \approx 2$ at $x = x_I$, which means that the instability is amplified by a factor e^2. This indicates that the flow is still in the beginning of the linear regime in this region. If the flow was initially laminar, the development of very small initial perturbations would not have been noticed. But the elliptic structures contain energetic perturbations which originate in the boundary layer. The strain field associated with the streamline ellipticity then amounts to a distortion of this turbulence to which it supplies energy and imposes a preferential orientation (see Cambon & Scott 1999).

To conclude, the above analysis suggests that the elliptic instability is responsible for the Gaussian-like distributions within the vortex centres of both the kinetic energy and the shear stress of the 'incoherent' fluctuations. This mechanism is thought to be one component of the onset of turbulence in a mixing layer. The second one, namely

amplification by stretching of perturbations located in the saddle, is also present, but it is revealed to be less active than in more standard mixing layers. This is probably a consequence of the strong two-dimensional organization of the present flow.

5. Conclusions

The unsteady shear layer developing over a deep cavity at high subsonic speed ($M = 0.8$) has been studied experimentally with a two-component laser-Doppler velocimeter. Phase-averaged quantities have been constructed by using an unsteady pressure signal measured in the cavity. A well-documented database has been obtained which contains a full description of the conditional statistics inside and around the cavity. Application of this conditional technique to such a high-speed flow was revealed to be a challenging task.

The analysis of the results led to the following main conclusions:

(*a*) The flow in this deep cavity, with an aspect ratio $L/D = 0.42$, is characterized by particularly strong self-sustain oscillations. The dominant frequency of these oscillations corresponds to the first cavity mode, the higher-order modes being closer to pure harmonics than those observed in shallower cavities.

(*b*) The possible influence of propagation and multi-reflection of acoustic fronts in the duct may contribute to selection of this particular regime, which departs from that described by the standard Rossiter model. Further experimental and/or numerical tests are necessary before drawing a definite conclusion.

(*c*) The dynamics of the flow above this cavity amounts to that of a mixing layer forced by an intense acoustic field at a frequency lower than the natural frequency of a mixing layer. Three different regions are identified from the mixing layer momentum thickness. A large growth rate, about three times that of equilibrium mixing layers, characterizes the region close to the separation point where the structures form. Then, the growth rate resumes a standard value whereas the flow regime strongly departs from a self-similar regime. A third region is where the flow structures interact with the downstream wall.

(*d*) The mixing layer rolls up into three well-defined vortices, following a scenario which bears some resemblance to the 'collective interaction mechanism' described by Ho & Nosseir (1981). Conditional analysis shows that this mechanism does not lock onto the fundamental frequency of the flow.

(*e*) These two-dimensional vortices possess their own convection speed and trajectory. They do not merge until they impact on the downstream edge of the cavity. The different behaviours of these structures in the downstream edge region determine the variation of the pressure at the edge.

(*f*) Second-order phase-averaged statistics show that more than half the kinetic energy is contained in the periodic components of the flow. The remainder, i.e. the 'incoherent' part, is preferentially located in the vortex centres. This result is in qualitative agreement with what is found in other free mixing layers.

(*g*) It is found that production of 'incoherent' velocity fluctuations is maximum in the centres and not in the saddle regions, a result which departs from the consensus on mixing layers. Elliptic instability is proposed as the mechanism responsible. In this strongly two-dimensional flow, amplification of the perturbations by the elliptic instability mechanism is found to be stronger than that due to vortex stretching in the saddles. This result is an indication that both mechanisms must be accounted for when considering the onset of three-dimensionality and turbulence in mixing layers.

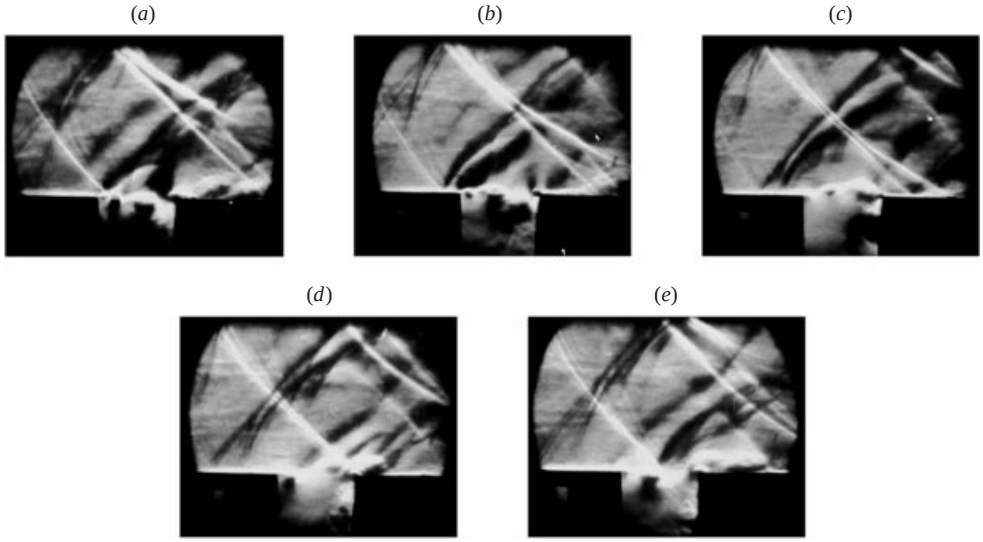

FIGURE 30. Visualization of one flow period (the time lag between each frame is 100 μs).

The present work was financially supported by the French Ministry of Defense (DGA/SPAé). The Measurement Group of the Fundamental/Experimental Aerodynamics Department of ONERA is thanked for their assistance in conducting the LDV measurements. Dr D. Sipp and Dr D. Fabre are acknowledged for their contribution to §4. Dr C. Pantano is also acknowledged for his help in reviewing the manuscript. The authors wish to thank the referees for comments and suggestions which contributed to strengthening this paper.

Appendix A. Acoustic wave reflection in the tunnel

A.1. *Visualizations*

Figure 30 shows a sequence of five schlieren pictures covering one period of the flow. One can distinguish in frame (*a*) the radiation of a wave packet from the cavity hole which looks like the early schlieren images shown by Krishnamurty (1955) in the case of small cavities in a very large wind tunnel test chamber. But one also observes upstream propagation of black and white fronts which are due to reflection on the tunnel walls. The resulting wave pattern amounts to the superposition of two saw-tooth waves that cross each other in the middle of the tunnel height. Figure 31 shows a series of five frames corresponding to the same phase but at different periods. This figure proves that the phenomenon is strictly periodic.

A.2. *Model*

The above observations may be explained by considering the following simplified model based on the image method.

Let $T_n = 1/f_n$ be the period of the nth cavity perturbation mode, of frequency f_n, emitted at point O. The wavelength of the perturbation is $\lambda_n = U_e/f_n$. After m periods, the perturbation has led to a wave train corresponding to the propagation of the original front and to its successive reflections from the two walls of the tunnel. Figure 32 corresponds to the case $n = 1$ and $m = 4$. If $\lambda_a^n = a_e/f_n$ denote the acoustic wavelength, with a_e the sound speed in the test section, after 4 periods, the original

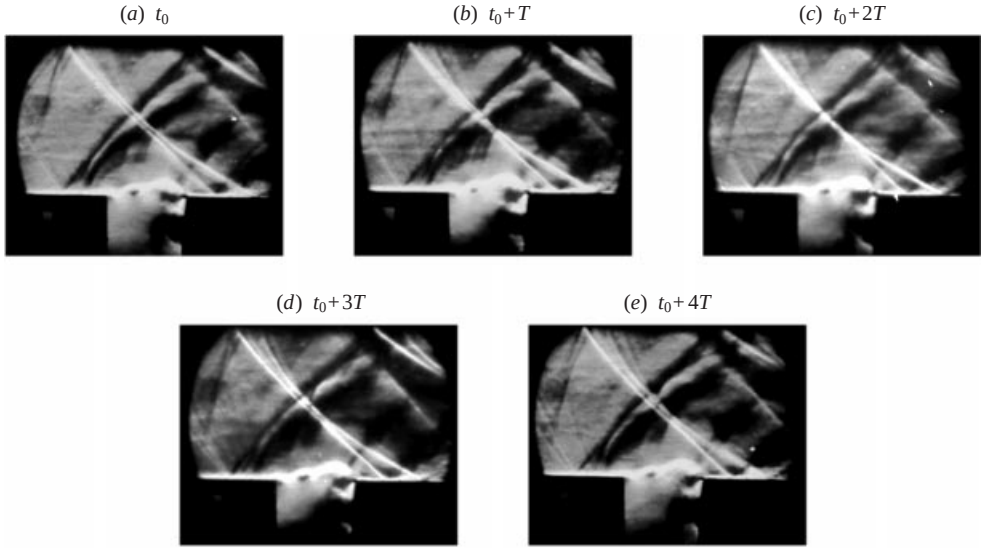

FIGURE 31. A series of frames corresponding to the same phase, see figure 30(*c*), at five successive flow periods.

front has been displaced upstream by a distance $4\lambda_a^n$ from a source which is located at $x = 4\lambda_n$. As sketched in the figure, six reflections take place. These reflections, numbered from $r = 1$ to 6, may be represented by considering the successive images of the original source with respect to the walls. The characteristic angle and the abscissa of points where reflection occurs are labelled θ_{rm}^n and x_{rm}^n, respectively. The following geometric relations hold:

$$x_{rm}^n = m\lambda_n \left[1 - \frac{\cos\theta_{rm}^n}{M}\right], \quad \sin\theta_{rm}^n = (-1)^{r+1}\frac{rh}{m\lambda_n/M}. \tag{A 1}$$

This gives

$$x_{rm}^n = m\lambda_n \left[1 - \frac{1}{M}\sqrt{1 - \left(\frac{rh}{m\lambda_n/M}\right)^2}\right]. \tag{A 2}$$

Introducing the Strouhal number $St_n = L/\lambda_n = f_n L/U_e$, one obtains

$$\frac{x_{rm}^n}{L} = \frac{m}{St_n}\left[1 - \frac{1}{M}\sqrt{1 - M^2\left(\frac{r}{m}\frac{h}{L}St_n\right)^2}\right]. \tag{A 3}$$

Relation (A 3) thus defines the abscissa where the reflected wave labelled r associated to the mth period of the perturbation impact the tunnel walls. Odd- (respectively even-) values of r correspond to impacts on the top wall, $y_{rm}^n = h$ (respectively, on the bottom wall, $y_{rm}^n = 0$). The complete wave train amounts to a superposition of the waves corresponding to all possible values of m, the period number, and of r, the reflection number. Different mode orders, n, may be accounted for, each one being characterized by a Strouhal St_n. Note that the total number of possible periods depends on the length of the tunnel portion, L_c, which separates the convergent section from the source, see figure 32. The positions of the leading wave fronts, x_{0m}^n,

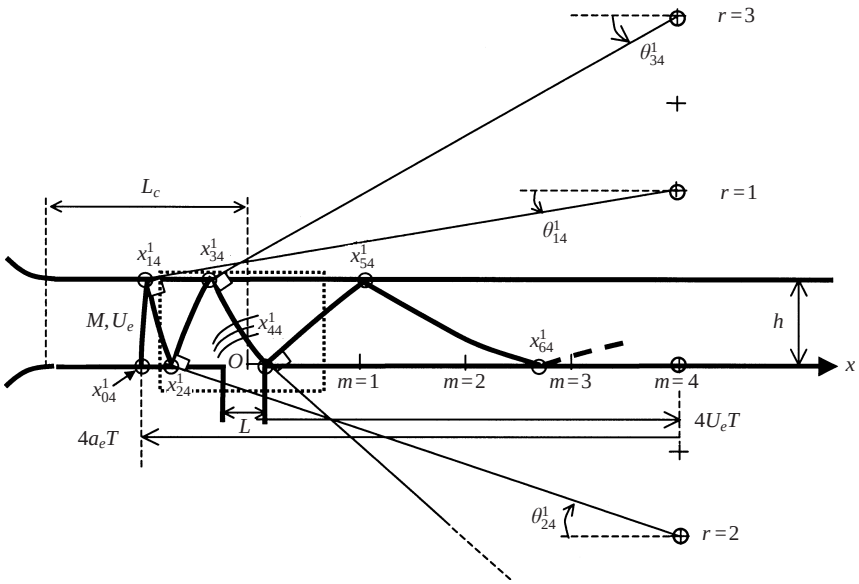

FIGURE 32. Wave patterns developing in the duct (image method): propagation and reflections after four periods T_1 of an acoustic front induced by a perturbation originating from point O with a period equal to $T_1 = 1/f_1$ (first cavity mode); the dotted rectangle shows the region visualized in figures 30 and 31.

must satisfy $|x^n_{0m}| < L_c$, the wave fronts corresponding to higher values of m being 'swallowed' by the convergent region. From (A 3), $|x^n_{0m}| = mL(1-M)/(MSt_n)$, so that the total number of periods is limited by the following relation:

$$m < \frac{M}{1-M} St_n \frac{L_c}{L}. \tag{A 4}$$

Given m, (A 3) limits also the maximum number of possible reflections to

$$r(m) \leqslant m \left(\frac{h}{L} MSt_n \right)^{-1}. \tag{A 5}$$

Indeed, the number of possible reflections is inversely proportional to the duct aspect ratio h/L (no reflection when $h/L \to \infty$) and to the Strouhal value. Combining (A 4) and (A 5), the maximum number of reflections in the duct is such that

$$r < \frac{L_c/h}{1-M}, \tag{A 6}$$

which introduces a dependence on the duct aspect ratio h/L_c.

In our case, the distance between the cavity upstream edge and the convergent is equal to 230 mm, see figure 1. The tunnel height is $h = 100$ mm and the cavity length, $L = 50$ mm. Let us consider, for instance, the case where the source is located at the downstream edge of the cavity, which means that $L_c = 280$ mm. For $St_1 \approx 0.375$, and $St_2 \approx 0.75$, which correspond to the strongest frequencies, (A 4) predicts 8 and 16 superimposed wave trains in the duct, respectively. From (A 5), we find that 13 reflections occur in both cases. The total number of reflected waves in the duct is limited to 14, whatever the Strouhal number, see (A 6).

We search now the conditions for focusing of these waves at the source origin.

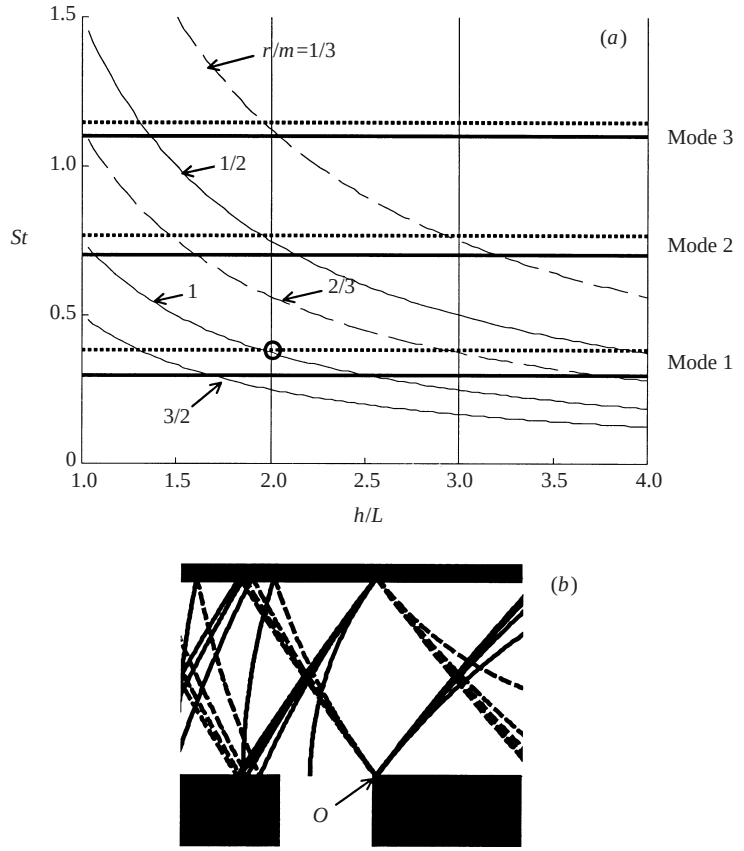

FIGURE 33. Focusing of reflected waves at the perturbation source at $M = 0.8$. The source is placed at the downstream edge of the cavity. (a) Influence of the tunnel height h/L: solutions of (A 7) (the horizontal solid lines are the Strouhal values deduced from the Rossiter model with ($\alpha = 0.25$, $U_c/U_e = 0.57$); the dotted lines are the values found in the present experiment, see symbols in figure 6). (b) Wave train obtained for $(h/L, St_1) = (2, 0.375)$, corresponding to the circle in (a). Full lines: leading fronts and reflections from the bottom; dotted lines: waves reflected from the top. The source origin, point O, is indicated.

We suppose, again, that the source is located at the downstream cavity edge. Putting $x^n_{rm} = 0$ in (A 3) selects Strouhal numbers such that

$$St_n = \frac{\sqrt{1 - M^2}}{M \dfrac{r}{m} \dfrac{h}{L}}, \tag{A 7}$$

where r/m is a rational number. Figure 33(a) shows the variation of St_n with h/L for the main rational values r/m. For $h/L = 2$, the figure clearly indicates a possible resonance with the first cavity mode of focused waves such that $r/m = 1$. In this case, modes 2 and 3 are also in correspondence with the focused waves $r/m = 1/2$ and $r/m = 1/3$, respectively. Consequently, the system also promotes the harmonics of the fundamental, e.g. the first one $St_2 = 2St_1$, as found in the present experiment. This is an indication that the above described mechanism could participate to the selection of the observed resonant frequencies, which are close to harmonics and slightly depart from the Rossiter modes.

Note that integer values of r/m, e.g. $r/m = 1$, are most effective because they enable focusing of a maximum number of waves: the reflection from the bottom, labelled $r = 2$, of the wave emitted after $m = 2$ periods coincides with reflection $r = 4$ of the wave $m = 4$ and so on, up to the last possible period fixed by (A 4). Waves corresponding to odd-values of r also collapse on the top wall at the source abscissa. For $St_1 \approx 0.375$ we saw that $m = 8$ periods are present in the duct. This means that four reflections coincide at the source for $r/m = 1$. This is illustrated in figure 33(b) which shows the result of a computation of the image method for $St_1 = 0.375$, $h/L = 2$ and $L_c/L = 5.6$. The waves are seen to collapse at the source within a quite well-defined wave pattern which looks, qualitatively, like those observed in figures 30 and 31. This wave pattern propagates upstream and deforms slightly, but the same is retrieved after each flow period.

Now, a detailed inspection of figure 33(b) shows that the wave pattern is narrower than those observed in figures 30 and 31. A better fit is obtained when the source is placed slightly upstream of the cavity, but there is no evident reason for a localization of the source here. This is an indication that the model is too simple to describe completely the mechanism. However, the model indicates that confinement effects are possibly contributing, somehow, to the global dynamics of the flow. This may occur when the reflected waves are periodically sweeping the upstream edge of the cavity where the shear layer separates. Other types of interaction, above and around the cavity, may also contribute. Note for instance that the waves which impact on the shear layer during propagation of the pattern are refracted within the cavity (this refraction process is clearly apparent in figure 12a, b). This introduces an acoustic front inside the cavity which could interfere with the cavity resonance.

Appendix B. Jitter

The purpose of this Appendix is to evaluate if jitter of the coherent structures could explain the unusual distribution of the shear stress. We show first that jitter is weak (away from the impingement region). We show then that, whatever its amplitude, jitter cannot explain the observed distribution of shear stress.

As we saw in § 3.7, the periodic motion is subjected to variations from period to period when approaching the downstream edge in region III. These deviations from periodicity are called jitter, see Hussain & Zaman (1980). Jitter may result from random shifts of the structure position (spatial jitter or meandering) and/or from variations of the field amplitude from period to period (temporal jitter). These effects cannot be avoided when the working signal and the conditioning signal are issued from different points in the flow, as in the present case. As discussed by Hussain (1986) and by Lyn *et al.* (1995), these variations of the coherent motion may contribute to the random part of the fluctuations. Interpretation of second-order statistics may then be obscured by this effect.

Thanks to the periodic nature of the flow and to the proximity of the two measurement points, we expect this effect to be weak, except in the downstream edge region. Figure 34 shows the phase-averaged random shear stress $-\langle u'w'\rangle$. The corresponding iso-levels of vorticity $\langle\Omega_y\rangle$ are found in figure 27(b). Important phase shifts between $\langle\Omega_y\rangle$ and $-\langle u'w'\rangle$ become evident in the vicinity of the wall. Note that, even if a slight smearing of $-\langle u'w'\rangle$ is found in the structures at the entrance of region III, a strong correlation with $\langle\Omega_y\rangle$ still remains there. This indicates that the relation between vorticity and random shear stress may be profoundly changed in regions where jitter occurs.

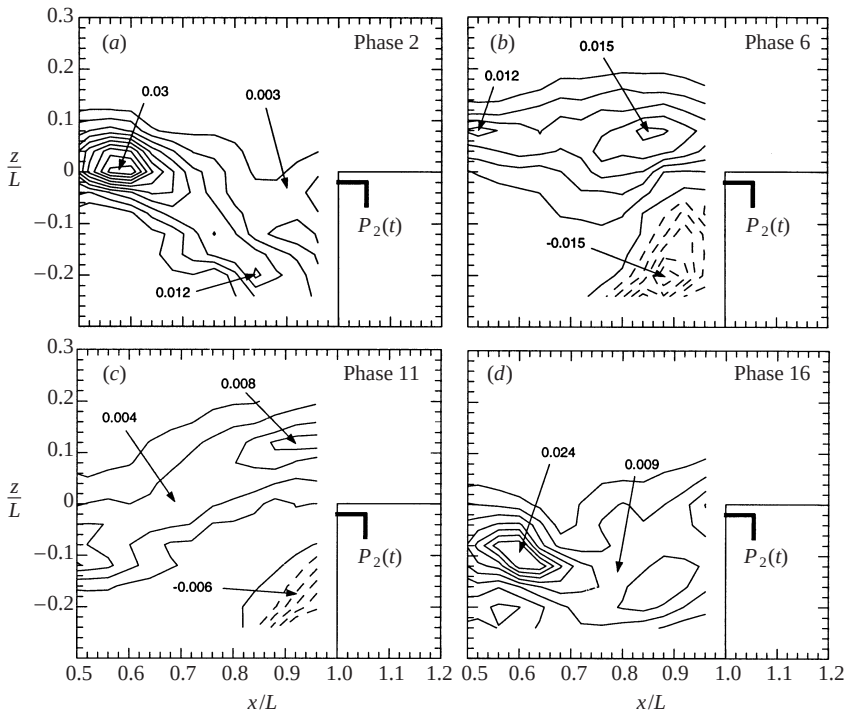

FIGURE 34. Contour plots of the phase-averaged random shear stress $-\langle u'w'\rangle/U_e^2$ for phase 2, 6, 11 and 16. The corresponding contour plots of the phase-averaged vorticity $\langle\Omega_y\rangle$ are shown in figure 27(*b*).

B.1. *Jitter evaluation*

Jitter may be evaluated by considering the spectra of the total and 'incoherent' velocity fluctuations. An example is given in figure 35 where the spectral densities and the co-spectra of the u- and w-velocity components deduced from LDV measurements at the centre of the shear layer, i.e. $x/L = 0.5$, $y = z = 0$, are shown. We used equal-time-spaced data obtained by means of a linear interpolation of the randomly spaced LDV samples. The integral under the spectra of figures 35(*a*) and 35(*b*) (dotted lines) corresponds to the Reynolds-averaged normal stresses $\overline{u_0'^2}$ and $\overline{w_0'^2}$. Figure 35(*c*) shows the absolute value of the real part of the co-spectrum, whose integral is equal to $-\overline{u_0'w_0'}$. The integrals under the spectra and co-spectra of the random fluctuations (full lines) correspond to $\overline{\langle u'^2\rangle}$, $\overline{\langle w'^2\rangle}$ and $\overline{\langle u'w'\rangle}$. Note that a linear interpolation of the data, such as that used here, leads to a progressive attenuation of the signal energy beyond frequencies equal to 1/5 to 1/6 the LDV mean sampling rate, see Ramon & Millan (2000). In the centre of the mixing layer, the mean sampling rate is nearly 25 kHz. Accordingly, an attenuation must be felt beyond $f \approx 4$ kHz, that is beyond $St \approx 0.75$. This does not change the integral values which are found to be close to those obtained from temporal averages of the LDV data signals. Moreover, this interpolation bias affects the full and the filtered data of figure 35 equivalently. Consequently, the latter can be compared without ambiguity on a larger frequency range.

The conditional analysis being phase locked on the first cavity mode, figure 35 shows that it leads to a strong reduction of the first energy peak. After integration, this peak was found to contain nearly two thirds of $\overline{u_0'^2}$, $\overline{w_0'^2}$ and $\overline{u_0'w_0'}$, in accordance with the results of § 3.6.

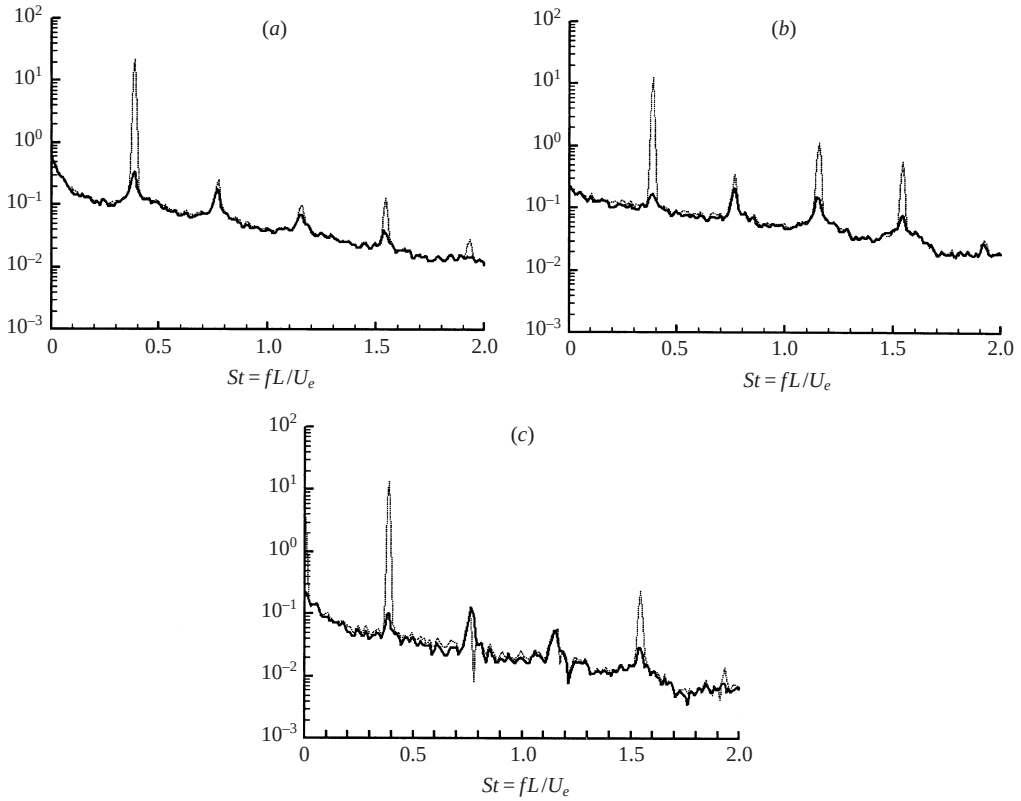

FIGURE 35. Spectral densities of the velocity field in the centre of the shear layer ($x/L = 0.5$, $y = z = 0$): (*a*) *u*-component, (*b*) *w*-component, (*c*) real part of the co-spectrum (absolute value). Dotted lines: full data, solid lines: 'incoherent' fluctuations.

However, figure 35 shows that part of the 'incoherent' energy comes from 'leakage' from the main frequency and its harmonics. But the remaining peaks are found to contribute less than 10% of the velocity energy $\overline{\langle u'^2 \rangle}$ or $\overline{\langle w'^2 \rangle}$. The same is true for the shear stress $-\overline{\langle u'w' \rangle}$. This means that, on average, less than 10% of $-\langle u'w' \rangle$ comes from 'leakage' from the main frequency and its harmonics into the incoherent fluctuations. This gives an evaluation of how much jitter contributes to $-\langle u'w' \rangle$.

B.2. *Simplified analysis of the contribution of jitter to the shear stress*

Here, we use another argument to show that, whatever its level, jitter cannot be responsible for the present distribution of $-\langle u'w' \rangle$. This argument is based on the observation that meandering of a vortex around its phase-averaged position cannot result in a Gaussian random shear stress distribution centred on the vortex axis, as is found here. This may be illustrated by considering, as in § 4.2, a Lamb–Oseen vortex with a vorticity distribution given by relation (9). Suppose now that this vortex structure is subjected to a random motion around its centre. Figure 36 shows the distribution of $-\langle u'w' \rangle$ obtained when the vortex is subjected to an isotropic random motion around its centre. This motion results in a perfectly quadripolar distribution. Non isotropic motions would also lead to a two-signed distribution of $-\langle u'w' \rangle$ with a minimum in the vortex centre. This contradicts our experimental

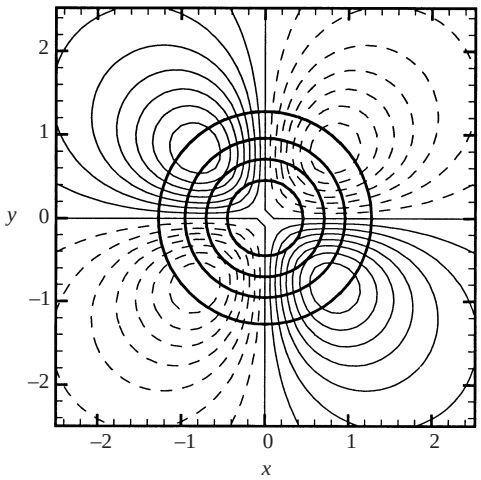

FIGURE 36. Meandering of a Lamb–Oseen vortex: iso-values of $-\langle u'w'\rangle(x,z)$ resulting from an isotropic motion of the vortex (arbitrary levels). The circles show the background vortex $\omega_y(x,z) = \exp\{-(x^2+z^2)\}$.

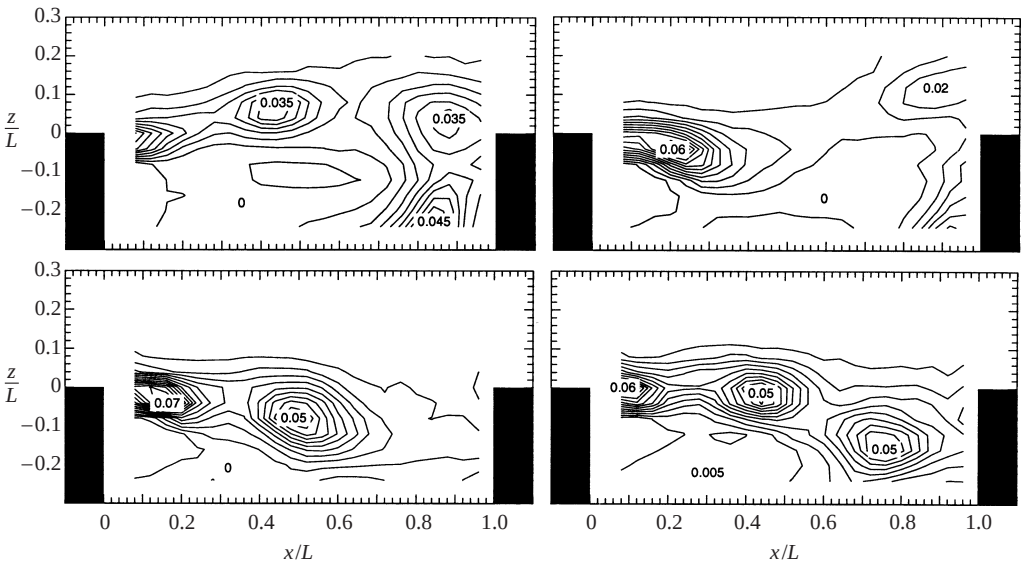

FIGURE 37. Contour plots of the phase-averaged Stokes number $\langle\tau\rangle$: (*a*) phase 5, (*b*) phase 10, (*c*) phase 15, (*d*) phase 20 (levels from 0 to 0.07 in increments of 0.005).

observations. An interesting comparison may be done with the flow corresponding to the trailing vortices of high-aspect-ratio wings. In these flows, one also observes that the perturbation kinetic energy undergoes a sharp and very local increase in the vortex centre, whereas $-\overline{u_0'w_0'}$ exhibits a quadripolar distribution such as that shown in figure 36; measurements have confirmed that fluctuations in such flows are entirely dominated by strong meandering of the vortices (Devenport *et al.* 1996; Jacquin *et al.* 2001).

The conclusion is that jitter is not responsible for the distribution of $-\langle u'w'\rangle$.

Appendix C. Particle bias

The purpose of this Appendix is to evaluate particle bias that could result from centrifugal motion by the coherent vortices of the mixing layer. A criterion for evaluating bias due to particle inertia in a mixing layer was provided by Samimy & Lele (1991) based on a two-dimensional DNS of the particle flow tracking accuracy and particle dispersion in a two-dimensional, mildly compressible, free shear layer. Considering particles with density, ρ_p and mean diameter d_p, particle inertia effects are evaluated through a Stokes number defined as $\tau = \tau_p/\tau_f$ where $\tau_p = \rho_p d_p^2/18\mu$ with μ the fluid viscosity and where τ_f is a flow time scale. In Samimy & Lele (1991), τ_f was evaluated as $\tau_f = 10\delta_{\omega_0}/(U_1 - U_2)$ with δ_{ω_0} the initial vorticity thickness and where 1 and 2 refer to high- and low-speed streams, respectively. They found that the velocity field provided by LDV measurements can be considered accurate when $\tau \leqslant 0.2$. In our case, $\rho_p \approx 10^3$ kg, $d_p \approx 0.6\,\mu$m, $\delta_{\omega_0} \approx 1$ mm, $U_1 = U_e \approx 260\,\mathrm{m\,s^{-1}}$ and $U_2 = 0$. This leads to $\tau_p \approx 1\,\mu$s, $\tau_f \approx 40\,\mu$s, $\tau = 0.025$. The latter value is much smaller than the limit $\tau = 0.2$ proposed by Samimy & Lele (1991).

However, due to the intermittent nature of the vorticity field in the present flow it might be preferable to consider smaller values of τ_f than that given above which may better account for centrifugal effects inside the coherent vortices. Conditional analysis provides an estimation for this time scale, namely $\langle\tau_f\rangle \approx 1/\langle\Omega_y\rangle_{max}$. According to figure 12, in the flow region covered by the measurements, an evaluation of $\langle\Omega_y\rangle_{max}$ is $\langle\Omega_y\rangle_{max}L/U_e \approx 20$, that is $1/\langle\Omega_y\rangle_{max} \approx 10\,\mu$s. This gives $\langle\tau\rangle \approx 0.1$. Figure 37 shows sample distributions of $\langle\tau\rangle$ for four different phases of the flow. As discussed in § 4.2, a final correction should be made to account for the mesh size effect, which leads to underestimation of $\langle\Omega_y\rangle_{max}$ by nearly a factor 2. This finally leads to $\langle\tau\rangle \approx 0.2$, for which measurements may be considered as valid following Samimy & Lele (1991).

The conclusion is that particle inertia effects are negligible.

REFERENCES

Ahuja, K. K. & Mendoza, J. 1995 Effects of cavity dimensions, boundary layer, and temperature on cavity noise with emphasis on benchmark data to validate computational aeroacoustic codes. *NASA Contractor Rep.* 4653.

Bayly, B. J. 1988 Three-dimensional instability of inviscid two-dimensional flows. *Phys. Fluids* **31**, 56–64.

Bilanin, A. J. & Covert, E. E. 1973 Estimation of possible excitation frequencies for shallow rectangular cavities. *AIAA J.* **11**, 347–351.

Browand, F. K. & Troutt, T. R. 1985 The turbulent mixing layer: geometry of large vortices. *J. Fluid Mech.* **158**, 489–509.

Cambon, C. & Scott, J. F. 1999 Linear and non-linear models of anisotropic turbulence. *Annu. Rev. Fluid Mech.* **31**, 1–53.

Cantwell, B. & Coles, D. 1983 An experimental study of entrainment and transport in the turbulent near wake of a circular cylinder. *J. Fluid Mech.* **136**, 321–374.

Cattafesta, L. N., Garg, S., Kegerise, M. A. & Jones, G. S. 1998 Experiments on compresssible flow-induced cavity oscillations. *AIAA Paper* 98-2912.

Colonius, T. 2001 An overview of simulation, modeling and active control of flow/acoustic resonance in open cavities. *AIAA Paper* 2001-0076.

Devenport, W. J., Rife, M. C., Liaps, S. I. & Follin, G. J. 1996 The structure and development of a wing tip vortex. *J. Fluid Mech.* **312**, 67–106.

Doty, M. J. & McLaughlin, D. K. 2000 Experiments on Mach wave interactions in a compressible shear layer. *AIAA J.* **38**, 1871–1878.

Forestier, N. 2000 Etude expérimentale d'une couche cisaillée au-dessus d'une cavité en régime transsonique. PhD thesis, Ecole Centrale de Lyon.

Forestier, N., Geffroy, P. & Jacquin, L. 1999 Flow over cavities in transonic regime: a test case for numerical simulations. *Proc. First Intl Symp. on Turbulence Shear Flow Phenomena*, Santa Barbara, CA, pp. 933–938.

Forestier, N., Geffroy, P. & Jacquin, L. 2000 Etude expérimentale des propriétés instationnaires d'une couche de mélange compressible sur une cavité: cas d'une cavité ouverte peu profonde. *Rapport Technique ONERA* RT 22/00153 DAFE.

Gharib, M. & Roshko, A. 1987 The effect of flow oscillations on cavity drag. *J. Fluid Mech.* **177**, 501–530.

Heller, H. H. & Bliss, D. B. 1975 The physical mechanism of flow-induce pressure fluctuations in cavities and concepts for their suppression. *AIAA Paper* 75-491.

Ho, C.-M. 1986 Mixing process in free shear layers. *AIAA Paper* 86-0234.

Ho, C.-M. & Huang, L.-S. 1982 Subharmonics and vortex merging in mixing layers. *J. Fluid Mech.* **119**, 443–473.

Ho, C.-M. & Huerre, P. 1984 Perturbed free shear layers. *Annu. Rev. Fluid Mech.* **16**, 365–424.

Ho, C.-M. & Nosseir, N. S. 1981 Dynamics of an impinging jet. Part 1. The feedback phenomenon. *J. Fluid Mech.* **105**, 119–142.

Huerre, P. & Monkewitz, P. 1985 Absolute and convective instabilities in free shear layers. *J. Fluid Mech.* **159**, 151–168.

Hussain, A. K. M. F. 1986 Coherent structures and turbulence. *J. Fluid Mech.* **173**, 303–356.

Hussain, A. K. M. F. & Hayakawa, M. 1987 Eduction of large-organized structures in a turbulent plane wake. *J. Fluid Mech.* **180**, 193–229.

Hussain, A. K. M. F. & Reynolds, W. C. 1970 The mechanics of an organized wave in turbulent shear flow. *J. Fluid Mech.* **41**, 241–258.

Hussain, A. K. M. F. & Zaman, K. B. M. Q. 1980 Vortex pairing in a circular jet under controlled excitation. Part 2. Coherent structure dynamics. *J. Fluid Mech.* **101**, 493–544.

Hussain, A. K. M. F. & Zaman, K. B. M. Q. 1985 An experimental study of organized motions in the turbulent plane mixing layer. *J. Fluid Mech.* **159**, 85–104.

Jacquin, L., Fabre, D., Geffroy, P. & Coustols, E. 2001 The properties of a transport aircraft wake in the extended near field: an experimental study. *AIAA Paper* 2001-1038.

Jacquin, L., Forestier, N. & Geffroy, P. 1998 Caractérisation expérimentale des propriétés instationnaires d'un écoulement au-dessus d'une cavité profonde en régime compressible ($M = 0,8$). *Rapport Technique ONERA* 9/2496 DAFE.

Jeong, J. & Hussain, A. K. M. F. 1995 On the identification of a vortex. *J. Fluid Mech.* **285**, 69–94.

Kegerise, M. A. 1999 An experimental investigation of flow-induced cavity oscillations. PhD thesis, Syracuse University.

Krishnamurty, K. 1955 Acoustic radiation from two-dimensional rectangular cut-outs in aerodynamics surfaces. *NACA TN* 3487.

Larchevêque, L., Sagaut, P., Mary, I., Labbé, O. & Comte, P. 2003 Large-eddy simulation of a compressible flow past a deep cavity. *Phys. Fluids* (in press).

Lyn, D. A., Einav, S., Rodi, W. & Park, J.-H. 1995 A laser-Doppler velocimetry study of ensemble-averaged characteristics of the turbulent near wake of a square cylinder. *J. Fluid Mech.* **304**, 285–319.

Lyn, D. A. & Rodi, W. 1994 The flapping shear layer formed by flow separation from the forward corner of a square cylinder. *J. Fluid Mech.* **267**, 353–376.

Meunier, P. & Leweke, T. 2001 Three-dimensional instability during vortex merging. *Phys. Fluids* **12**, 10, 2747–2750.

Moore, D. W. & Saffman, P. G. 1975 The instability of a straight vortex filament in a strain field. *Proc. R. Soc. Lond.* A **346**, 413–425.

Oster, D. & Wygnanski, I. 1982 The forced mixing layer between parallel streams. *J. Fluid Mech.* **123**, 91–130.

Pierrehumbert, R. T. 1986 Universal short-wave instability of two dimensional eddies in an inviscid fluid. *Phys. Rev. Lett.* **57**, 2157–2159.

Pierrehumbert, R. T. & Widnall, S. E. 1982 The two- and three-dimensional instabilities of a spatially periodic shear layer. *J. Fluid Mech.* **114**, 59–82.

Plumblee, H. E., Gibson, J. S. & Lassiter, L. W. 1962 A theoretical and experimental investigation of the acoustic response of cavities in an aerodynamic flow. *US Air Force*, WADD-TR-61-75.

Ramon, A. & Millan, P. 2000 Measurements and treatment of LDA signals, comparisons with hot-wire signals. *Exps. Fluids* **28**, 58–63.

Rockwell, D. & Knisely, C. 1979 The organised nature of flow impingement upon a corner. *J. Fluid Mech.* **93**, 413–432.

Rockwell, D. & Naudascher, E. 1979 Self-sustained oscillations of impinging free shear layers. *Annu. Rev. Fluid Mech.* **11**, 67–94.

Rossiter, J. E. 1964 Wind-tunnel experiments on the flow over rectangular cavities at subsonic and transonic speeds. *Aeronaut. Res. Coun. R. & M.* 3438, October 1964.

Rowley, C. W., Colonius, T. & Basu, A. J. 2002 On the self-sustained oscillations in two-dimensional compressible flow over rectangular cavities. *J. Fluid Mech.* **455**, 315–346.

Samimy, M. & Lele, S. K. 1991 Motion of particles with inertia in a compressible free shear layer. *Phys. Fluids* A **3**, 1915–1923.

Sipp, D., Coppens, F. & Jacquin, L. 1999 Theoretical and numerical analysis of wake vortices. In *ESAIM Proc.* Vol. 7, pp. 397–407, *Third Internal Workshop on Vortex Flows and Related Numerical Methods*. See also *European* Series in Applied and Industrial Mathematics (ESAIM). www.emath.fr/Maths/proc.

Tam, C. K. W. & Block, P. J. W. 1978 On the tones and pressure oscillations induced by flow over rectangular cavities. *J. Fluid Mech.* **89**, 373–399.

Tang, Y. P. & Rockwell, D. 1983 Instantaneous pressure fields at a corner associated with vortex impingement. *J. Fluid Mech.* **126**, 187–204.

Waleffe, F. 1990 On the three-dimensional instability of strained vortices. *Phys. Fluids* A **2**, 76–80.

Winant, C. D. & Browand, F. K. 1974 Vortex pairing, the mechanism of turbulent mixing layer growth at moderate Reynolds number. *J. Fluid Mech.* **63**, 237–255.

Zhang, X. & Edwards, J. A. 1990 An investigation of supersonic oscillatory cavity flows driven by thick shear layers. *Aeronaut. J.* **100**, 355–364.